

Dust-to-neutral gas ratio of the intermediate and high velocity H I clouds derived based on the sub-mm dust emission for the whole sky

Takahiro Hayakawa,¹* and Yasuo Fukui¹

¹*Department of Physics, Nagoya University, Furo-cho Chikusa-ku, Nagoya 464-8602, Japan*

Accepted XXX. Received YYY; in original form ZZZ

ABSTRACT

We derived the dust-to-H I ratio of the intermediate-velocity clouds (IVCs), the high-velocity clouds (HVCs), and the local H I gas, by carrying out a multiple-regression analysis of the 21 cm H I emission combined with the sub-mm dust optical depth. The method covers over 80 per cent of the sky contiguously at a resolution of 47 arcmin and is distinguished from the absorption line measurements toward bright galaxies and stars covering a tiny fraction of the sky. Major results include that the ratio of the IVCs is in a range of 0.1–1.5 with a mode at 0.6 (relative to the solar-neighbourhood value, likewise below) and that a significant fraction, ~ 20 per cent, of the IVCs include dust-poor gas with a ratio of < 0.5 . It is confirmed that 50 per cent of the HVC Complex C has a ratio of < 0.3 , and that the Magellanic Stream has the lowest ratio with a mode at ~ 0.1 . The results prove that some IVCs have low metallicity gas, contrary to the previous absorption line measurements. Considering that the recent works show that the IVCs are interacting and exchanging momentum with the high-metallicity Galactic halo gas, we argue that the high-metallicity gas contaminates a significant fraction of the IVCs. Accordingly, we argue that the IVCs include a significant fraction of the low metallicity gas supplied from outside the Galaxy as an alternative to the Galactic-fountain model.

Key words: ISM: abundance – ISM: atoms – ISM: clouds — Galaxy: halo

1 INTRODUCTION

The high-velocity clouds (HVCs) and their slower-moving counterparts, the intermediate-velocity clouds (IVCs), are H I clouds with large velocities that a simple model of the Galactic rotation can not explain. Typically observed at positions distant from the Galactic plane and predominantly in a negative radial velocity range. The early discoveries were made over a half-century ago (e.g., Munch 1952; Münch & Zirin 1961; Muller et al. 1963; Smith 1963; Blaauw & Tolbert 1966; see a review by Wakker et al. 2004 for research history up to 1999). There have been several efforts to constrain the distance to the IVCs/HVCs using the absorption-line bracketing technique. The IVCs are located relatively close, and have typical z heights of ~ 1 –2 kpc (e.g., Wakker et al. 2008; Lehner et al. 2022, see also compilations by Wakker 2001; van Woerden & Wakker 2004 and references therein), and are likely to be the disc-halo interface objects, while the major HVCs are further away, several to ~ 10 kpc above the disc (e.g., van Woerden et al. 1999; Thom et al. 2006, 2008; Wakker et al. 2007, 2008; Smoker et al. 2011; Richter et al. 2015; Lehner et al. 2022) and belong to the inner halo. One of the important questions is whether the IVCs and HVCs are different halo-cloud populations (i.e., gas comes from the disc, and the one fuels the disc) or just the same population of objects with different heights and radial velocities.

The metallicity is a crucial parameter for pursuing the origin and has traditionally been measured by observing absorption lines. The previous works presented that the prominent HVCs in the Complexes

A and C have sub-solar metallicities $Z/Z_{\odot} \sim 0.1$ –0.3 (Richter et al. 2001b; Tripp et al. 2003; Collins et al. 2003, 2007; Sembach et al. 2004; Fox et al. 2023, see also compilations by Wakker 2001) and are of extra-galactic origin. The IVCs have been reported to have near-solar metallicity of ~ 0.5 –1.0 solar (Wakker 2001 and references therein; Richter et al. 2001a,b; Sembach et al. 2004) and are usually explained by the so-called Galactic-fountain model in which hot gas ejected from the disc by the stellar feedback falls back in the form of neutral clouds (Shapiro & Field 1976; Bregman 1980). However, the measured metallicities often have rather large uncertainties due to such factors as ionization states and interstellar depletion (van Woerden & Wakker 2004 summarised the possible problems in the metallicity determination in their section 5). In addition, these measurements are made at a limited number of locations because of a tiny number of bright background objects and do not lead to firmly establish the metallicity of the IVC.

An alternative method for measuring metallicity is to use dust emissions. It is a reasonable proxy for absorption measurements because the dust consists of a significant fraction of heavy elements, perhaps comparable to that in the gas phase (see also discussion in Section 5.1). For this purpose, the $100 \mu\text{m}$ emission obtained with *IRAS* is often used. However, it is not a valid measure of the interstellar dust mass. In the Rayleigh-Jeans regime, all components having various temperatures in a line-of-sight contribute to the emission proportionally to their masses, whereas lower-temperature components contribute little in the Wien regime. Generally, only in the Rayleigh-Jeans regime can we measure all dust mass. In interstellar dust, the peak wavelength of the modified Planck function is around $100 \mu\text{m}$, and the sub-mm wavelength satisfies the Rayleigh-Jeans regime. The

* E-mail: t.hayakawa@a.phys.nagoya-u.ac.jp (TH)

Planck Collaboration obtained such sensitive sub-mm dust emission over the whole sky at a 5 arcmin resolution and derived dust optical depth at 353 GHz (850 μm), τ_{353} , by fitting the modified Planck function at four wavelengths from 100 to 850 μm obtained by *Planck* and *IRAS* (Planck Collaboration XI 2014; Planck Collaboration Int. XLVIII 2016).

Previous works by Fukui et al. (2014, 2015, F14 and F15 hereafter), Okamoto et al. (2017, O17), Hayashi et al. (2019a, H19), and Hayashi et al. (2019b) showed that τ_{353} characterises well the linearity of the dust emission in a number of regions of the Milky Way. The scheme was also applied to the Large Magellanic Cloud (LMC). As such, Fukui et al. (2017, F17) used the linear relationship between the velocity-integrated intensity of H I line, $W_{\text{H I}}$, and τ_{353} , and estimated that the H I ridge including R136 has a factor of two lower dust-to-H I ratio than the optical stellar Bar region in LMC. In addition, Tsuge et al. (2019, T19) presented that the N44 region near the H I Ridge in the LMC has a ~ 30 per cent lower dust-to-H I ratio than that of the Bar region. Most recently, Fukui et al. (2021, F21 hereafter) applied the method to IVC 86–36 in the Pegasus-Pisces (PP) Arch and derived a dust-to-H I ratio relative to the low-velocity (LV) ISM (considered to be in the solar neighbourhood) of ~ 0.2 , strongly suggesting that PP Arch originated in a dust-poor environment but not in the disc. Their measurements of the dust-to-gas ratio significantly improved the preceding metallicity measurements by optical/ultraviolet atomic absorption lines of the background stellar spectrum in the IVC (Fitzpatrick & Spitzer 1997). Although the absorption-line results suggest the subsolar metal abundance, the abundance values vary by ~ 0.5 dex depending on the atomic species, leaving the metallicity unquantified. Considering the whole above, we judge the dust-to-H I ratio measurements (F17; T19; F21) to be most appropriate and adopt it in the present work with an aim to extend the metallicity measurement of the H I gas over the whole sky outside the Galactic plane.

The aim of the present paper is to use τ_{353} and the 21 cm H I emission and to derive the dust-to-H I ratio in the IVCs and possibly the other H I components. It is not yet examined well if the low column density H I gas in the IVCs and HVCs have similar dust properties to the Galactic disc, and the extension of the dust emission to the halo H I gas is a challenge. Nonetheless, we believe that the paper benefits the community by reporting possible new aspects of the dust emission in these H I gases as well as the evolutionary trend of the Galactic ISM. The H I is an important mass reservoir, while the ionized gas may carry a large mass similar to the neutral H I gas. We focus on the neutral H I gas in the present paper because the dust-to-gas ratio in H I is one of the essential factors giving information on the chemical evolution. The paper is organized as follows: Section 2 describes the datasets used, and Section 3 gives the dust and gas properties analysed by the present work. Section 4 shows the dust-to-H I ratio distribution in middle/high latitudes including the individual outstanding components. Section 5 gives a discussion focusing on the implications of the IVC dust-to-H I ratio. Section 6 concludes the present work.

2 DATASETS

We used archival H I data from the HI4PI full-sky survey (HI4PI Collaboration 2016) and *Planck* PR2 dust data (Planck Collaboration Int. XLVIII 2016). Both are on the HEALPIX¹ (Górski et al.

2005) projection, and we performed the following analyses without reprojection. The HEALPIX is a framework for the pixelization of the data on the sphere. Unlike general regular grid maps, the resolution of a HEALPIX map is defined by the resolution parameter N_{side} (generally a power of 2). The map has $12N_{\text{side}}^2$ pixels of the same area over the whole sky, i.e., each pixel has a solid angle of $4\pi/(12N_{\text{side}}^2)$ sr. See section 4 of Górski et al. (2005) for further details, and refer to table 1 in the same publication for the correspondence between N_{side} and mean pixel spacing.

2.1 H I data

The HI4PI data combines those from the first release of the Effelsberg-Bonn H I Survey (EBHIS, Winkel et al. 2016) and the third revision of the Galactic All-Sky Survey (GASS, Kalberla & Haud 2015). The brightness temperature noise level is ~ 43 mK (rms) at a velocity resolution of 1.49 km s^{-1} . The velocity coverage (with respect to the Local Standard of Rest, LSR) is $|V_{\text{LSR}}| \leq 600 \text{ km s}^{-1}$ (EBHIS part) or $|V_{\text{LSR}}| \leq 470 \text{ km s}^{-1}$ (GASS part). The FWHM angular resolution of the combined map is 16.2 arcmin, twice better than the Leiden/Argentine/Bonn (LAB) Survey (Kalberla et al. 2005). The data are divided into 19 parts, and each of them is presented as a FITS binary table containing spectra on the HEALPIX grid with $N_{\text{side}} = 1024$ (the mean pixel spacing is 3.4 arcmin).

2.2 Dust optical depth data

Planck Collaboration Int. XLVIII (2016) used *Planck* 2015 data release (PR2) maps and separated Galactic thermal dust emission from cosmic infrared background anisotropies by implementing the generalized needlet internal linear combination (GNILC) method. The GNILC dust maps have a variable angular resolution with an effective beam FWHM varying from 5 to 21.8 arcmin (see fig. 2 of Planck Collaboration Int. XLVIII 2016). The authors then produced the dust optical depth, temperature, and spectral index maps by fitting a modified blackbody model to the GNILC dust maps at 353, 545, 857 GHz, and *IRAS* 100 μm map. We used the τ_{353} data released version R2.01 in the HEALPIX format with $N_{\text{side}} = 2048$ (the mean pixel spacing is 1.7 arcmin). The median relative uncertainty in τ_{353} is $\sigma(\tau_{353})/\tau_{353} = 0.037$ in $|b| > 15^\circ$.

Note that O17, H19², F17, T19 and F21 used *Planck* 2013 data release (PR1) dust data released version R1.20 (Planck Collaboration XI 2014), whereas Hayashi et al. (2019b) and the present study used the Planck Collaboration Int. XLVIII (2016) data. We compared the two datasets and found a good consistency between them (see Appendix A).

2.3 Pre-processing of the data

Figure 1 shows the Galactic longitude-LSR velocity diagrams for H I in both low latitudes ($|b| < 15^\circ$) and middle/high latitudes ($|b| > 15^\circ$). The diagrams reveal the Galactic-rotational motion in the former while indicating negligibly observable rotation in the latter. Therefore, we used the LSR velocity to define the IVCs in the

² The description in section 2.3 of H19, ‘released version R1.10 are used’, is to be corrected to ‘released version R1.20 are used’ (Hayashi, private communication).

¹ <http://healpix.sourceforge.net/>

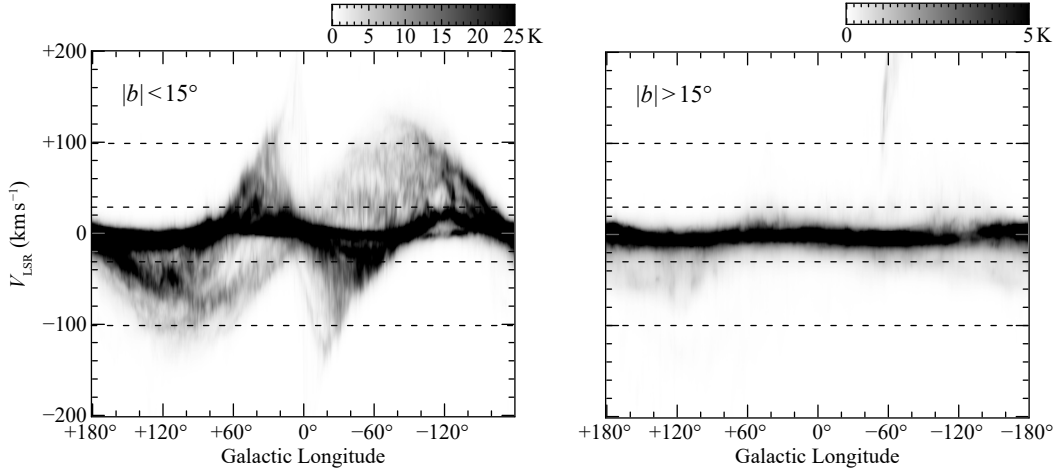


Figure 1. Galactic longitude-LSR velocity diagrams of the H I in $|b| < 15^\circ$ (left) and $|b| > 15^\circ$ (right) from the HI4PI data (HI4PI Collaboration 2016). The intensity is averaged over Galactic latitude. The horizontal dashed lines in each panel indicate $V_{\text{LSR}} = +100, +30, -30,$ and -100 km s^{-1} (from upper to lower).

middle/high latitudes rather than a deviation velocity³. Figure 1 also demonstrates that the LV components in the middle/high latitude are concentrated around $V_{\text{LSR}} = 0 \text{ km s}^{-1}$ and fall well within a range of $|V_{\text{LSR}}| < 30 \text{ km s}^{-1}$. F15 reported that more than 80 per cent of H I in $|b| > 15^\circ$ are in a V_{LSR} range from -9 to $+6 \text{ km s}^{-1}$ and have 1σ velocity dispersion of smaller than 10 km s^{-1} (see section 2.2 of F15). We set the boundary between the LV and the intermediate-velocity components at $|V_{\text{LSR}}| = 30 \text{ km s}^{-1}$. There is no explicit definition of the boundary between the IVCs and the HVCs, and values such as $|V_{\text{LSR}}| = 90 \text{ km s}^{-1}$ (e.g., Wakker 2001; Lehner et al. 2022) or 100 km s^{-1} (e.g., Röhser et al. 2016; French et al. 2021) are usually adopted. We have opted for a boundary value of 100 km s^{-1} in the present study. A straight cut in the LSR velocity frame can misclassify the objects having velocities near the boundary in some directions of the sky. It causes a loss of accuracy in the dust-to-H I ratio measurements, but we have not considered the loss in the present study.

The H I data were integrated into the five velocity ranges (summarized in Table 1) and combined into a single HEALPIX format data for each velocity range. The HI4PI H I and the *Planck* dust data have different resolutions, and we matched them as follows: (1) if the resolution of the *Planck* data is 21.8 arcmin at a data point, the H I data were smoothed, (2) otherwise ($5.0, 8.7, 11.7,$ or 15.0 arcmin), the dust data were smoothed to 16.2 arcmin resolution. Then both were degraded to $N_{\text{side}} = 256$ (the mean pixel spacing is 13.7 arcmin) to reduce the computational cost. In the following sections, we used these processed data unless otherwise noted.

3 NEUTRAL GAS AND DUST OPTICAL DEPTH PROPERTIES

Fig. 2 shows the spatial distributions of $W_{\text{H I}}$ in the negative (i.e., blue-shifted) intermediate velocity (NIV, $V_{\text{LSR}} = -100$ – -30 km s^{-1}), positive (red-shifted) intermediate velocity (PIV, $V_{\text{LSR}} = +30$ – $+100 \text{ km s}^{-1}$), and LV ($|V_{\text{LSR}}| < 30 \text{ km s}^{-1}$) components, respectively. Those of the negative- and positive high-velocity (NHV and

PHV, $|V_{\text{LSR}}| > 100 \text{ km s}^{-1}$) components are also shown as silhouettes. Fig. 3 shows the distribution function of the apparent amount (the product of the column density and the solid angle) of H I gas,

$$\sum_i N_{\text{H I}, X}^*(l_i, b_i) s \quad (1)$$

as a function of the column density,

$$N_{\text{H I}, X}^*(l_i, b_i) = C_0 W_{\text{H I}, X}(l_i, b_i), \quad (2)$$

where $X = \text{NHV, NIV, } \dots, \text{PHV}$ represents the velocity ranges listed in Table 1, (l_i, b_i) are the galactic coordinates of the i -th pixel ($i = 1, 2, \dots$), and $C_0 = 1.82 \times 10^{18} \text{ (cm}^{-2} \text{ K}^{-1} \text{ km}^{-1} \text{ s)}$. The solid angle of each pixel is given by $s = 4\pi/(12N_{\text{side}}^2) \text{ sr}$, and $N_{\text{side}} = 256$ in the present dataset. The asterisk put on $N_{\text{H I}}$ means the H I column density is under the optically-thin approximation (optical depth $\tau_{\text{H I}} \ll 1$), following the notation of F14, F15, O17 and H19. As reported in the previous works, the IVCs are mainly in the negative velocity range. The NIV components are concentrated in giant IVC complexes Intermediate-Velocity (IV) Arch, IV Spur, Low-Latitude (LL) IV Arch, and Complex M occupying one-third of $b > 15^\circ$ skies. Another prominent IVC, PP Arch, is located in the Galactic South and has a head-tail structure elongated from IVC 86 -36 to $(l, b) = (150^\circ, -60^\circ)$. The only small apparent amount of H I gas is in the positive velocity ranges, except for the Magellanic System. The LV components covering the whole sky are considered to be the local volume gas within 300 pc of the sun. They have an H I column density range of 10^{20} – 10^{21} cm^{-2} with a peak at 3 – $4 \times 10^{20} \text{ cm}^{-2}$, which is one order of magnitude higher than IVCs (1×10^{19} to $2 \times 10^{20} \text{ cm}^{-2}$) and HVCs ($\lesssim 1 \times 10^{20} \text{ cm}^{-2}$).

Fig. 4 shows the spatial distribution of τ_{353} , and Fig. 5 shows the correlation plots between τ_{353} and $W_{\text{H I}}$ in the $|b| > 15^\circ$ skies with masking described in Section 4.1. Here, the $W_{\text{H I}}$ values are velocity-decomposed, but the τ_{353} values are not. The good correlation between the two quantities is found only in the LV component, while the other components show a rather poor correlation. The plots demonstrate that the LV component dominates τ_{353} in almost every single direction, consistent with the remarkably similar spatial distribution of the LV H I gas (Fig. 2(c)) and τ_{353} (Fig. 4). Fig. 5 also presents nearly vertical features displaced or broadened along the τ_{353} axis in the high- and intermediate-velocity components. It indicates that dust-poor HV/IV H I overlaps with the dust-rich LV H I.

³ The deviation velocity is the difference between the velocity of a cloud and the nearest limit of the velocity allowed by a model of the galactic rotation toward the direction, introduced by Wakker (1991) for low latitudes.

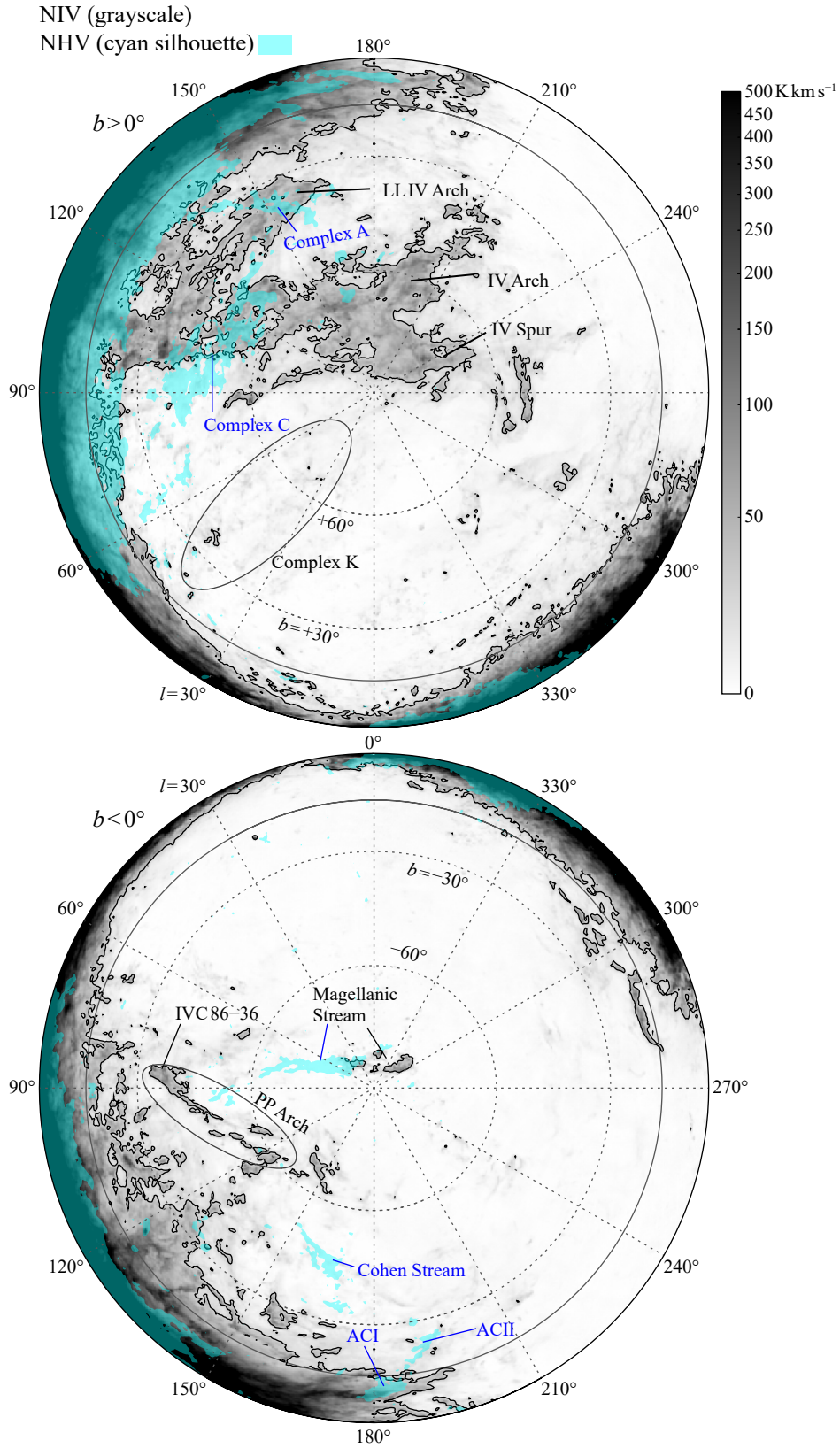


Figure 2. (a) The greyscale image shows the spatial distribution of H I integrated intensity in the NIV velocity range ($V_{\text{LSR}} = -100$ – -30 km s^{-1} , see Table 1), $W_{\text{H I, NIV}}$, in a zenithal equal area (ZEA) projection (HI4PI Collaboration 2016). The contours show $W_{\text{H I, NIV}} = 30 \text{ K km s}^{-1}$. The overlaid cyan silhouette shows the NHV components ($V_{\text{LSR}} = -470$ – -100 km s^{-1}) with $W_{\text{H I, NHV}} > 10 \text{ K km s}^{-1}$. Upper panels cover $b > 0^\circ$ and longitude increases clockwise. Lower panels cover $b < 0^\circ$ and longitude increases counterclockwise. Both join at $(l, b) = (0^\circ, 0^\circ)$. The grey solid lines indicate $|b| = 15^\circ$.

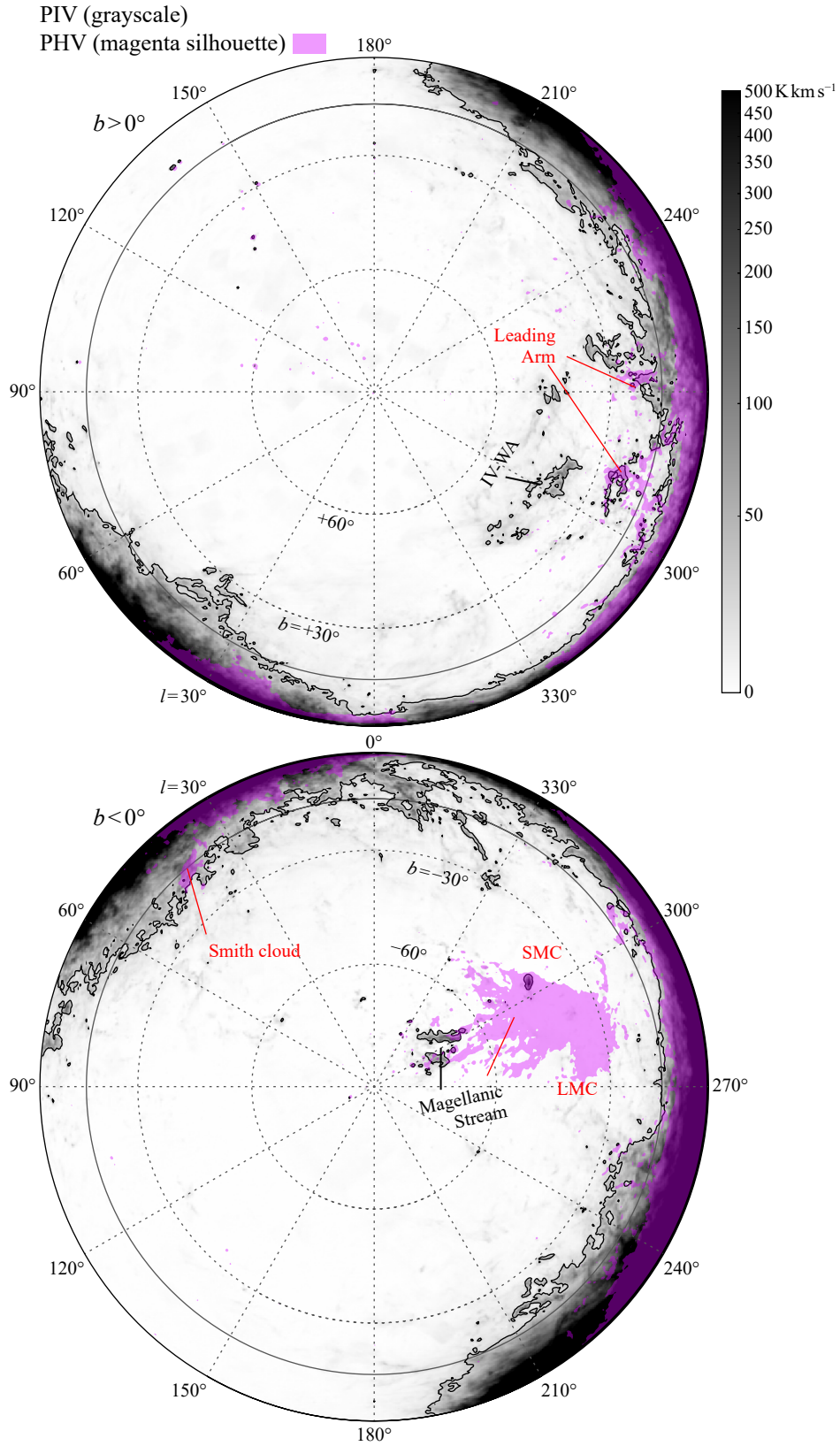


Figure 2 – *continued* (b) The greyscale image shows the PIV components ($V_{\text{LSR}} = +30\text{--}+100 \text{ km s}^{-1}$) and the contours show $W_{\text{H I, PIV}} = 30 \text{ K km s}^{-1}$. The overlaid magenta silhouette shows the PHV components ($V_{\text{LSR}} = +100\text{--}+470 \text{ km s}^{-1}$) with $W_{\text{H I, PHV}} > 10 \text{ K km s}^{-1}$.

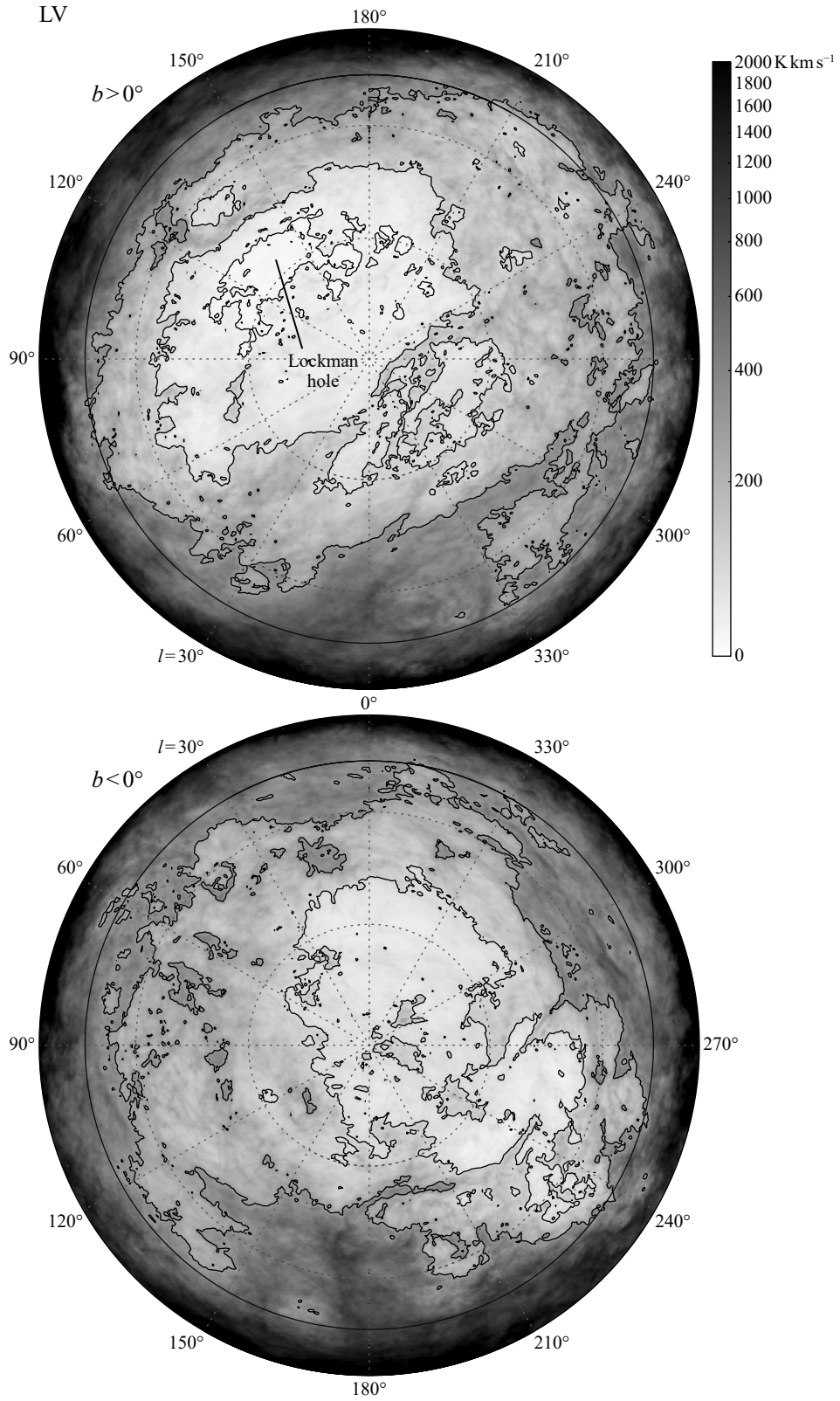


Figure 2 – continued (c) The greyscale image shows the LV components ($V_{\text{LSR}} = -30$ – $+30 \text{ km s}^{-1}$) and the contours show $W_{\text{HI,LV}} = 30, 100, \text{ and } 300 \text{ K km s}^{-1}$.

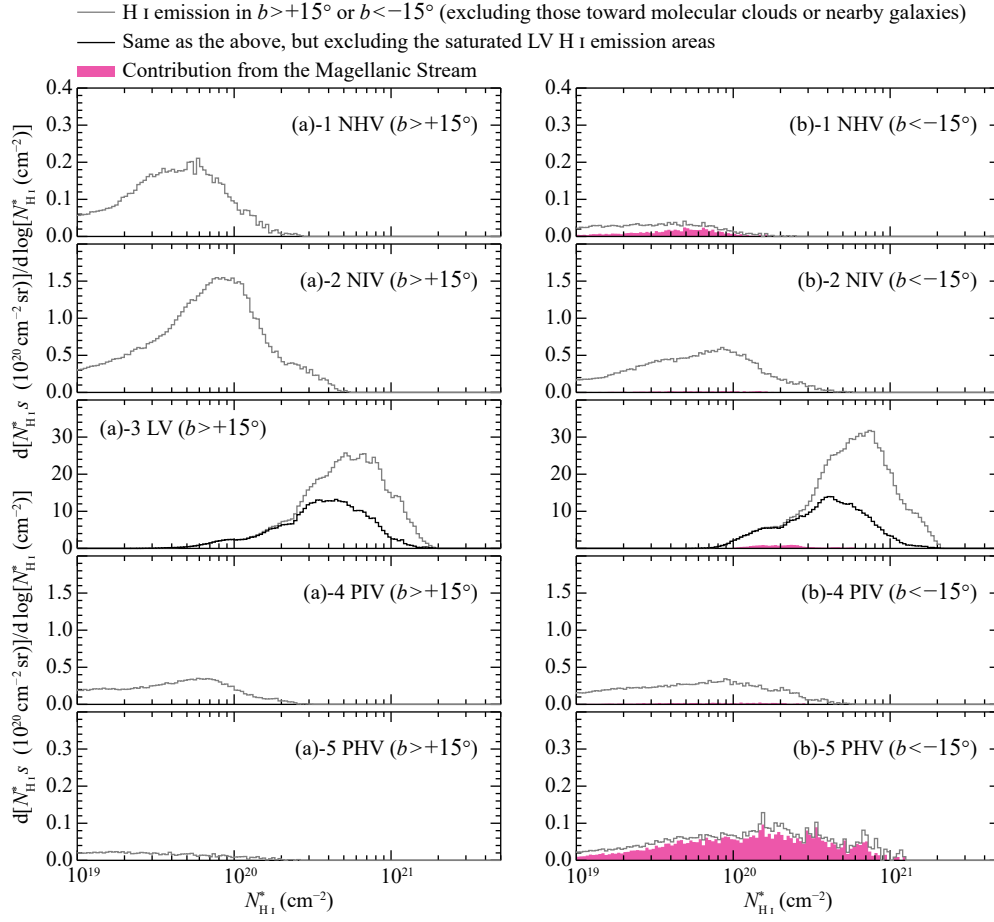


Figure 3. Distribution of the apparent amount of H I gas (the product of the column density and the solid angle, $N_{\text{H I}}^* X^s$) as a function of the column density under the optically thin approximation $N_{\text{H I}}^*$ (equation (2)) in the NHV, NIV, LV, PIV and PHV velocity ranges (from top to bottom), excluding toward molecular clouds or nearby galaxies (see Section 4.1). The panels in the left column are for $b > +15^\circ$, and those in the right column are for $b < -15^\circ$. The black lines in panels (a)-3 and (b)-3 further exclude the saturated LV H I emission (see Section 4.3). The shades in magenta show the contribution from the Magellanic Stream.

Table 1. Summary of the velocity ranges in the present study.

Name ^a	V_{LSR} range ^b (km s^{-1})	$N_{\text{H I}}^* s$ ($ b > 15^\circ$) ^c ($\text{cm}^{-2} \text{sr}$)	$N_{\text{H I}}^* s$ (with confident $\hat{\zeta}$) ^d ($\text{cm}^{-2} \text{sr}$)	
Negative high velocity (NHV)	-470 – -100	2×10^{19}	2×10^{18}	10%
Negative intermediate velocity (NIV)	-100 – -30	2×10^{20}	5×10^{19}	28%
Low velocity (LV)	-30 – +30	4×10^{21}	2×10^{21}	40%
Positive intermediate velocity (PIV)	+30 – +100	7×10^{19}	9×10^{18}	13%
Positive high velocity (PHV)	+100 – +470	5×10^{18}	3×10^{17}	6%

^a Identification name and its abbreviation form in parentheses.

^b Minimum and maximum velocities with respect to the LSR.

^c The total apparent amount of H I gas obtained by equation (1) in $|b| > 15^\circ$ skys excluding the Magellanic Stream.

^d The total apparent amount of H I gas of the pixels with $\sigma(\hat{\zeta})/\hat{\zeta}_{\text{soln}}$ better than 0.1 and the percentage of above.

4 THE ESTIMATE OF THE DUST-TO-H I RATIO

The present work uses $W_{\text{H I}}$ and τ_{353} to derive the dust-to-H I ratio in the LV, IVC and HVC components separately. The basic concept introduced in the previous studies (F17; T19; F21) is that the regression coefficient of a single regression between $W_{\text{H I}}$ and τ_{353} (or the gradient of the best-fit line in the $W_{\text{H I}}-\tau_{353}$ plane) gives the dust-to-H I ratio. However, in the framework of the present study, τ_{353} is

the sum of the contribution from the five velocity components, and it is impossible to estimate each ratio by a single regression between, e.g., $W_{\text{H I, NIV}}$ and a velocity-decomposed $\tau_{353, \text{H I, NIV}}$. Assuming that τ_{353} is a linear combination of multiple $W_{\text{H I, X}}$ -terms (see Section 4.2), we can estimate the dust-to-H I ratios of all components simultaneously as the partial coefficients of a multiple regression, or the gradient of the best-fit “plane” in an $(m + 1)$ -dimensional space,

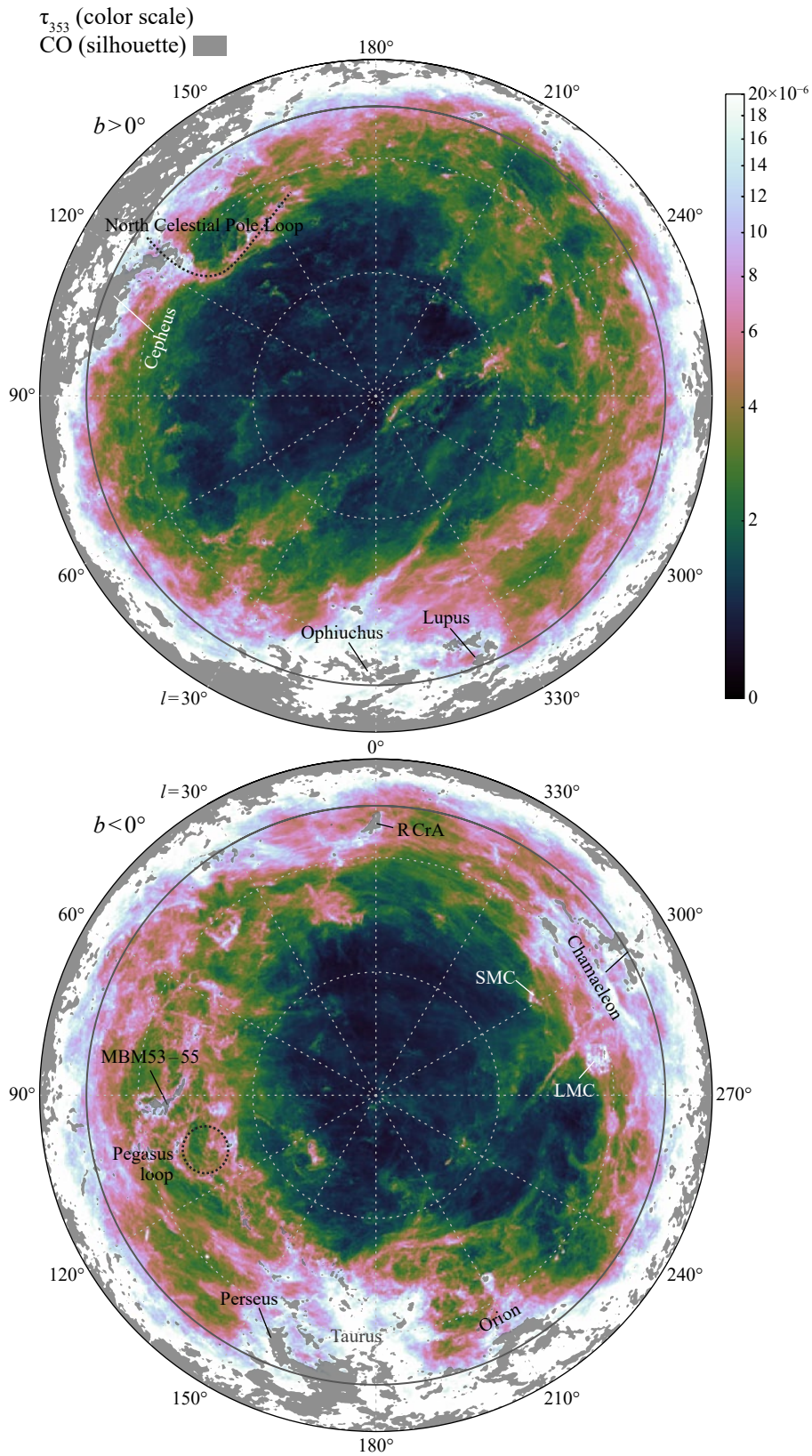


Figure 4. Spatial distribution of 353 GHz dust optical depth (τ_{353}) (Planck Collaboration Int. XLVIII 2016) shown in the same projection as Fig. 2. The overlaid silhouette outlines the molecular clouds with $W_{\text{CO}} > 1.4 \text{ K km s}^{-1}$ (Planck Collaboration X 2016).

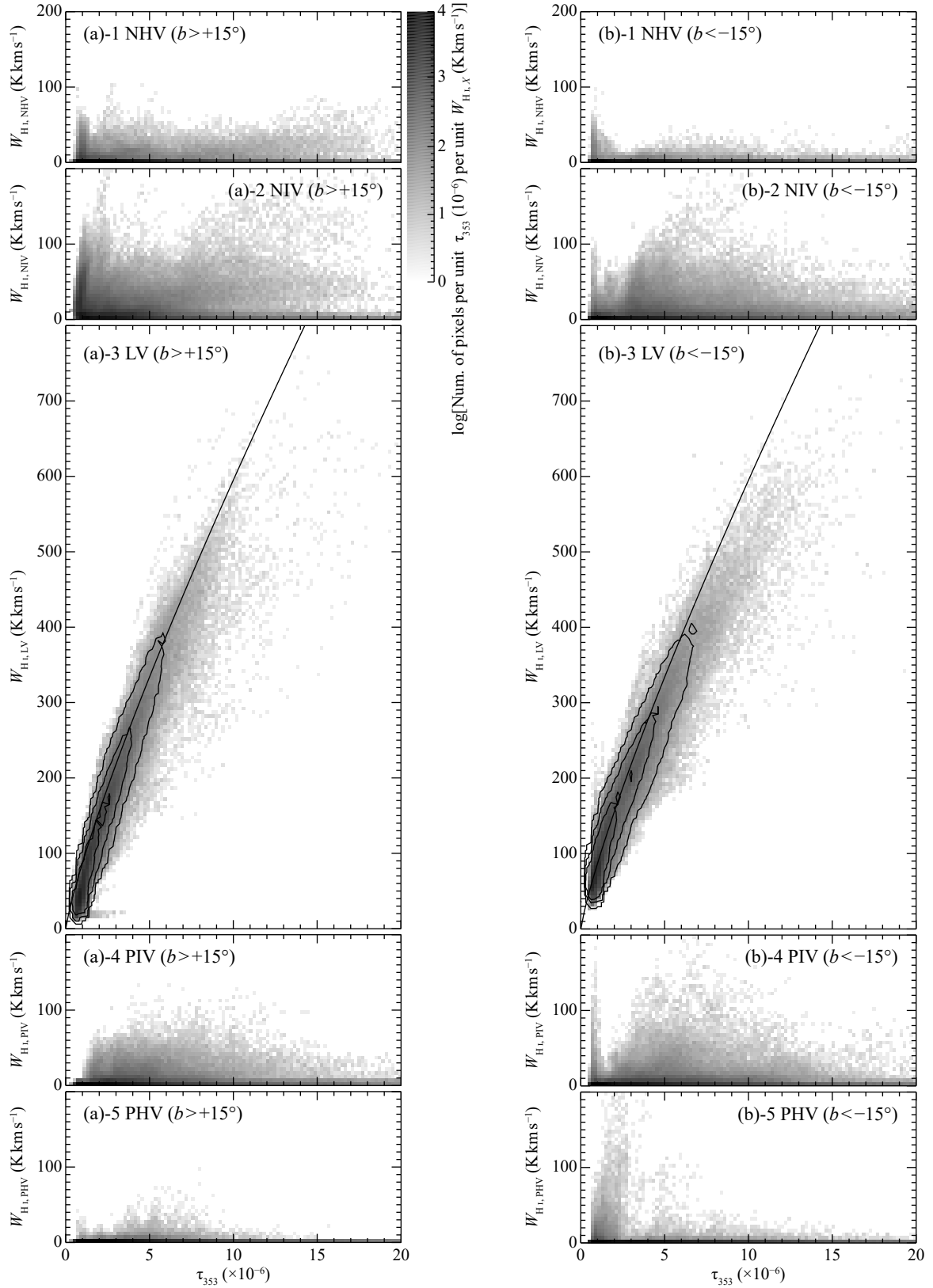


Figure 5. Density plots showing the correlation between τ_{353} and W_{HI} in the NHV, NIV, LV, PIV and PHV velocity ranges (from top to bottom), excluding toward molecular clouds or nearby galaxies (see Section 4.1). The plots in panels (a)-3 and (b)-3 further exclude the saturated LV H I (see Section 4.3). The W_{HI} values are obtained by integrating within each velocity range, but τ_{353} values are the total amount on the line-of-sights (not velocity-decomposed). The panels in the left column are for $b > +15^\circ$ and those in the right column are for $b < -15^\circ$. The contours panels (a)-3 and (b)-3 contain 50, 75 and 90 per cent of data points. The solid lines indicate the solar-neighbourhood dust-to-H I ratio (ζ_{soln}) line in this work $W_{\text{HI}} \text{ (K km s}^{-1}\text{)} = (1.59 \times 10^{25}) / (1.82 \times 10^{18}) \times \tau_{353}^{1/1.2}$ (see Section 4).

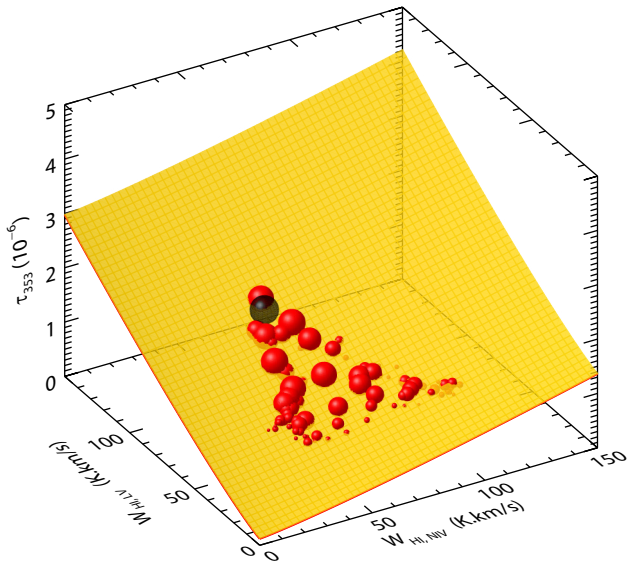


Figure 6. A toy model of the regression analysis. The 3D scatter plot in the $W_{\text{HI,NIV}}-W_{\text{HI,LV}}-\tau_{353}$ space shows the data points at and in the neighbour of a regression point $(l, b) = (150^\circ, +67^\circ)$ (the black sphere and the red ones, respectively). The radius of each sphere is proportional to the $1/3$ power of the weight given by equation (9) (decays with the angular distance in the sky from the regression point, maximum is 1.0 and truncated below 10^{-3}). The $W_{\text{HI,NHV}}$, $W_{\text{HI,PIV}}$, and $W_{\text{HI,PHV}}$ are small enough for these data points, and the contribution from these components to τ_{353} can be regarded as zero. The best-fit surface given by equation (8) with $\tilde{\zeta}_{\text{NIV}}(150^\circ, +67^\circ)/\zeta_{\text{soln}} = 0.70 \pm 0.09$ and $\tilde{\zeta}_{\text{LV}}(150^\circ, +67^\circ)/\zeta_{\text{soln}} = 1.40 \pm 0.08$ is also shown.

where m is the number of the $W_{\text{HI},X}$ terms and $m = 5$ in the present study.

The dust-to-H I ratio of each velocity component is not uniform across the sky, and we, therefore, used the geographically weighted regression (GWR) technique (Brunsdon et al. 1996; Fotheringham et al. 2002) which allows us to derive the spatial distribution of the dust-to-H I ratio, whereas the general regression estimates a set of global and spatially-invariant coefficients. The GWR technique is an outgrowth of the ordinary least-squares (OLS) regression. It is an advanced extension of the moving-window technique and estimates local coefficients at each pixel using a distance-decay weighting function.

Figure 6 is a visualization of the regression-analysis process at a regression point (a pixel where we want to estimate the local coefficients) $(l, b) = (150^\circ, +67^\circ)$, in a three-dimensional ($W_{\text{HI,LV}}-W_{\text{HI,NIV}}-\tau_{353}$) space⁴. We find that the “plane”⁵ immediately gives the two gradients $\tau_{353}-W_{\text{HI,LV}}$ and $\tau_{353}-W_{\text{HI,NIV}}$, and these gradients give the dust-to-H I ratios of the LV and NIV component, respectively.

As presented in Section 3, τ_{353} is dominated by the LV component, with $\sim 1-2$ orders smaller contributions from the other components. One might wonder whether extracting such faint and reduced contributions is possible. The issue could be severe if we subtract the

⁴ We made the regressions between the five H I terms and τ_{353} , as described in the following subsections, but $W_{\text{HI,NHV}}$, $W_{\text{HI,PIV}}$ and $W_{\text{HI,PHV}}$ are negligible in many cases.

⁵ The best-fit “plane” is slightly curved due to the small non-linearity of the sub-mm emission by the dust growth as expressed by an exponent $\alpha = 1.2$ (see Section 4.2).

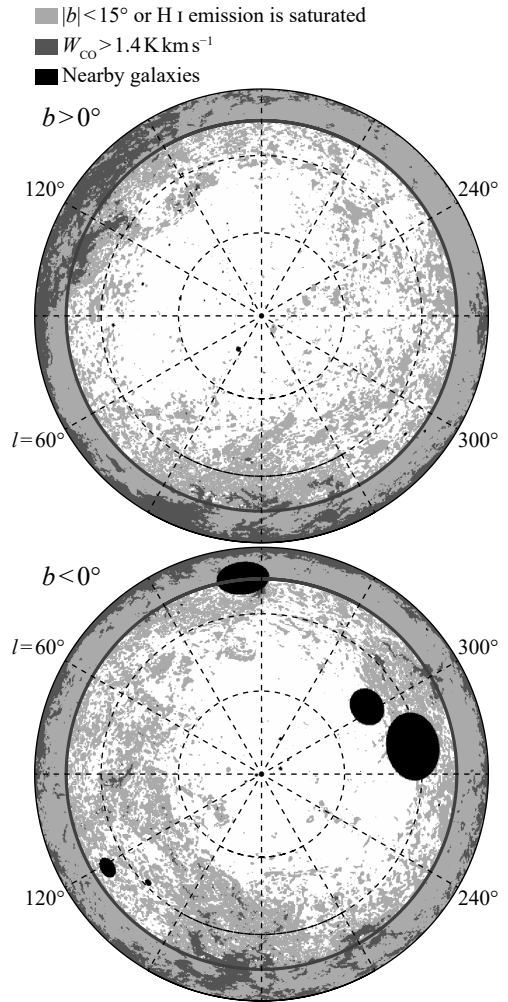


Figure 7. The masked and saturated H I areas in the present study (Sections 4.1 and 4.3) shown in the same projection as Fig. 2. The low latitude zone $|b| < 15^\circ$ is delimited by thick solid lines. The dark-grey shadow outlines the area with $W_{\text{CO}} > 1.4 \text{ K km s}^{-1}$ (Planck Collaboration X 2016). The black-filled ellipses cover nearby galaxies taken from the catalogue by Karachentsev et al. (2013) and samples studied by Wang et al. (2016). The light-grey shadow in $|b| > 15^\circ$ presents the areas where LV H I emission is saturated.

contribution from the LV component and analyze the remaining, as done in F21. In the present method, if we explain using the above model, the gradients in the $W_{\text{HI,NIV}}$ and $W_{\text{HI,LV}}$ directions are mutually independent, and it does not matter that the LV is dominant in τ_{353} . The uncertainty of τ_{353} ($\sigma(\tau_{353})$, typically on the order of 10^{-8} in the directions analyzed) probably provides the extraction limit in the present method. The HVCs, Magellanic Stream and some IVCs (such as PP-Arch) are close to the limit (typically estimated to be several $\times 10^{-8}$), whereas the IVC complexes IV Arch/Spur have large enough τ_{353} ($\gtrsim 10^{-7}$) (see also Section 4.3).

4.1 Masking

The pixels which meet any of the criteria (a)–(c) were masked before the regression analysis;

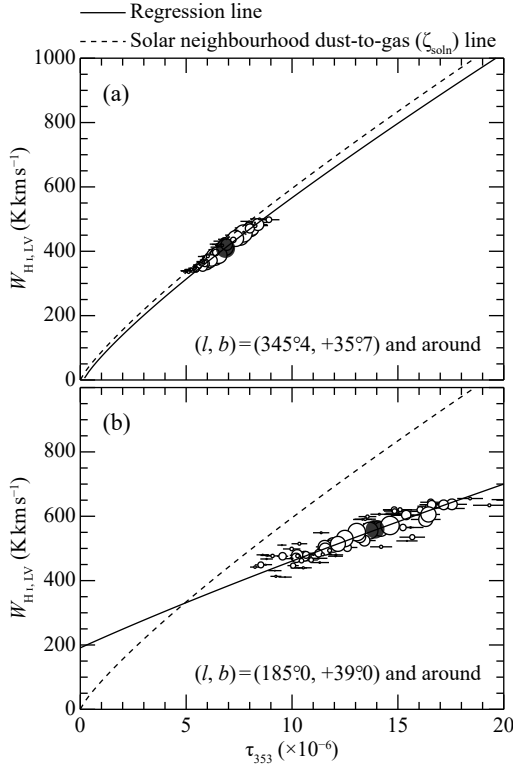


Figure 8. (a) Scatter plot showing the τ_{353} - $W_{\text{H I, LV}}$ correlation for data points at and in the neighbour (within 1.2 deg) of a regression point $(l, b) = (345^\circ.4, +35^\circ.7)$ where the LV H I emission is judged to be optically thin (not saturated). The filled circle is the data point at the regression point, and the open circles are those in the neighbour. The radius of each circle is proportional to the $1/2$ power of the weight given by equation (9), (decays with the angular distance in the sky from the regression point, maximum is 1.0 and truncated below 10^{-3}). The horizontal bars attached to the data points show $\sigma(\tau_{353})$ (Planck Collaboration Int. XLVIII 2016). The solid lines show local regression lines described by equation (8) at the position. The dashed line indicates the solar-neighbourhood dust-to-H I ratio (ζ_{soln}) line in this work (see Section 4). (b) Same as (a) but for data points within 1.2 deg of $(l, b) = (185^\circ.0, -39^\circ.0)$ where the LV H I emission is judged to be saturated. In both samples, the H I integrated intensity of the NHV, NIV, PIV, and PHV components are small enough ($W_{\text{H I, X}} < 5.5 \text{ K km s}^{-1}$ or $N_{\text{H I, X}}^* < 1 \times 10^{19} \text{ cm}^{-2}$), and their contribution to τ_{353} is approximately zero.

(a) Galactic latitude is $|b| < 15^\circ$ in order to eliminate contamination by the Galactic-disc components far from us.

(b) CO emission is detected at the 3σ level (1.4 K km s^{-1}), where the molecular gas is not negligible compared to the atomic gas. We used the *Planck* PR2 type 2 CO(1–0) map (Planck Collaboration X 2016). The median uncertainty of the map is $\sigma(W_{\text{CO}}) = 0.44 \text{ K km s}^{-1}$ in $|b| > 15^\circ$.

(c) The areas covering nearby galaxies listed in either or both the catalogue by Karachentsev et al. (2013) and the samples studied by Wang et al. (2016).

Fig. 7 summarises the masked areas.

4.2 Formulation

The observed τ_{353} is the sum of the contribution from each component,

$$\tau_{353}(l_i, b_i) = \sum_X \tau_{353, \text{H}^+, \text{X}}(l_i, b_i) + \sum_X \tau_{353, \text{H I, X}}(l_i, b_i) + \sum_X \tau_{353, \text{H}_2, \text{X}}(l_i, b_i), \quad (3)$$

where $\tau_{353, \text{H}^+, \text{X}}$, $\tau_{353, \text{H I, X}}$, and $\tau_{353, \text{H}_2, \text{X}}$ are the contribution from the dust associated with ionized, atomic, and molecular gas in the velocity range X , respectively. The molecular fraction can be approximated to be zero in the unmasked regions. If we assume that the contribution from the ionized component is negligibly small (see also discussion in Section 5.2), then equation (3) can be rewritten as

$$\tau_{353}(l_i, b_i) = \sum_X \tau_{353, \text{H I, X}}(l_i, b_i). \quad (4)$$

The contribution from a component X is expressed as a function of its H I column-density $N_{\text{H I, X}}$, introducing a dust-to-H I ratio parameter ζ ,

$$\tau_{353, \text{H I, X}}(l_i, b_i) = [\zeta_X(l_i, b_i) N_{\text{H I, X}}(l_i, b_i)]^\alpha. \quad (5)$$

We used a $N_{\text{H I}}$ model having a nonlinear relationship with τ_{353} found by O17 and H19. These authors used the 21 cm H I data with τ_{353} following F14 and F15 by taking into account the optical depth effect of the 21 cm H I emission. O17 derived a τ_{353} - $N_{\text{H I}}$ relationship with $\alpha = 1.3$ for the H I gas in the Perseus region, and H19 obtained $\alpha = 1.2$ in the Chamaeleon molecular cloud complex. The value of α greater than 1.0 was suggested to be due to the dust evolution effect by Roy et al. (2013) who derived the non-linearity with $\alpha = 1.3$ from (the far infrared optical depth)-(near infrared colour excess) relationship in Orion. Hayashi et al. (2019b) made a *Fermi*-LAT γ -ray analysis and confirmed the non-linearity with $\alpha \sim 1.4$. In the following analyses, we adopted $\alpha = 1.2$.

The H I column density is a function of $W_{\text{H I, X}}$ and H I optical depth $\tau_{\text{H I, X}}$,

$$N_{\text{H I, X}}(l_i, b_i) = C_0 \frac{\tau_{\text{H I, X}}(l_i, b_i)}{1 - \exp[-\tau_{\text{H I, X}}(l_i, b_i)]} W_{\text{H I, X}}(l_i, b_i). \quad (6)$$

As it is not feasible to simultaneously estimate both $\zeta_X(l_i, b_i)$ and $\tau_{\text{H I, X}}(l_i, b_i)$ as free parameters in a regression model due to the compounded relationship arising from their multiplication, we assume that

$$N_{\text{H I, X}}(l_i, b_i) \sim N_{\text{H I, X}}^*(l_i, b_i) = C_0 W_{\text{H I, X}}(l_i, b_i) \quad (7)$$

under the optically thin approximation of the H I emission ($\tau_{\text{H I, X}} \ll 1$) (see Section 4.3 for exception handling for optically thick cases). Then, we set up the regression equation using equations (4), (5) and (7) as

$$\tau_{353}(l_i, b_i) = \tau_{353, 0}(l_i, b_i) + C_0^\alpha \sum_X [\zeta_X(l_i, b_i) W_{\text{H I, X}}(l_i, b_i)]^\alpha. \quad (8)$$

The constant term $\tau_{353, 0}(l_i, b_i)$ is the amount of τ_{353} unaffected by variation in $W_{\text{H I, X}}$, e.g., the zero-level offsets (see also discussion in Section 5.2), and has been found empirically to take far off from zero if H I emission is saturated due to the optical depth effect (Fig. 8).

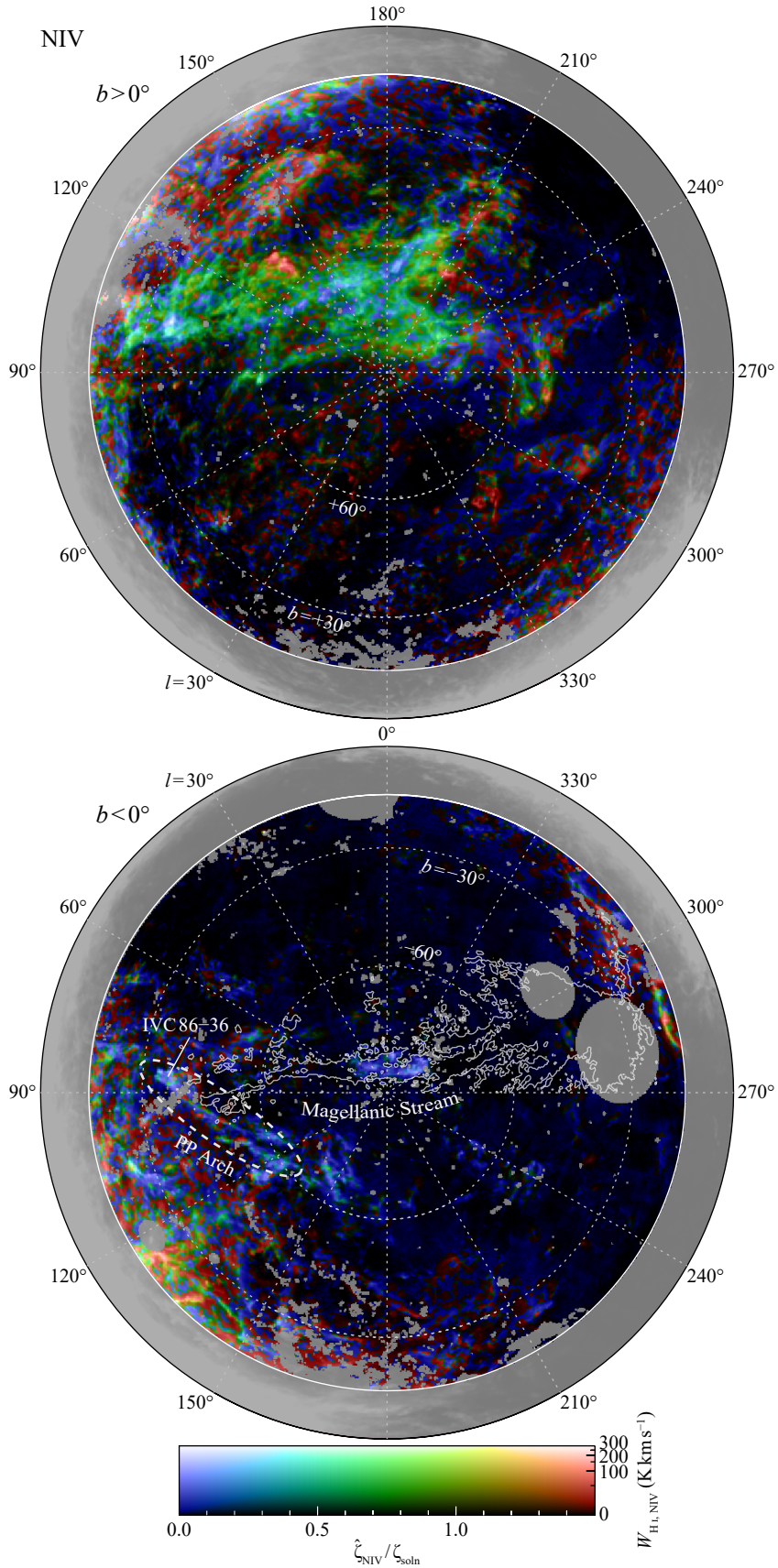


Figure 9. (a) Spatial distribution of the relative dust-to-H I ratio $\widehat{\zeta}_{\text{NIV}} / \zeta_{\text{soln}}$ encoded as colour hue and $W_{\text{H I, NIV}}$ presented by brightness, shown in the same projection as Fig. 2. The grey shadow presents the areas with no valid $\widehat{\zeta}_{\text{NIV}}$ values. The white contours in the lower panel outline the Magellanic Stream.

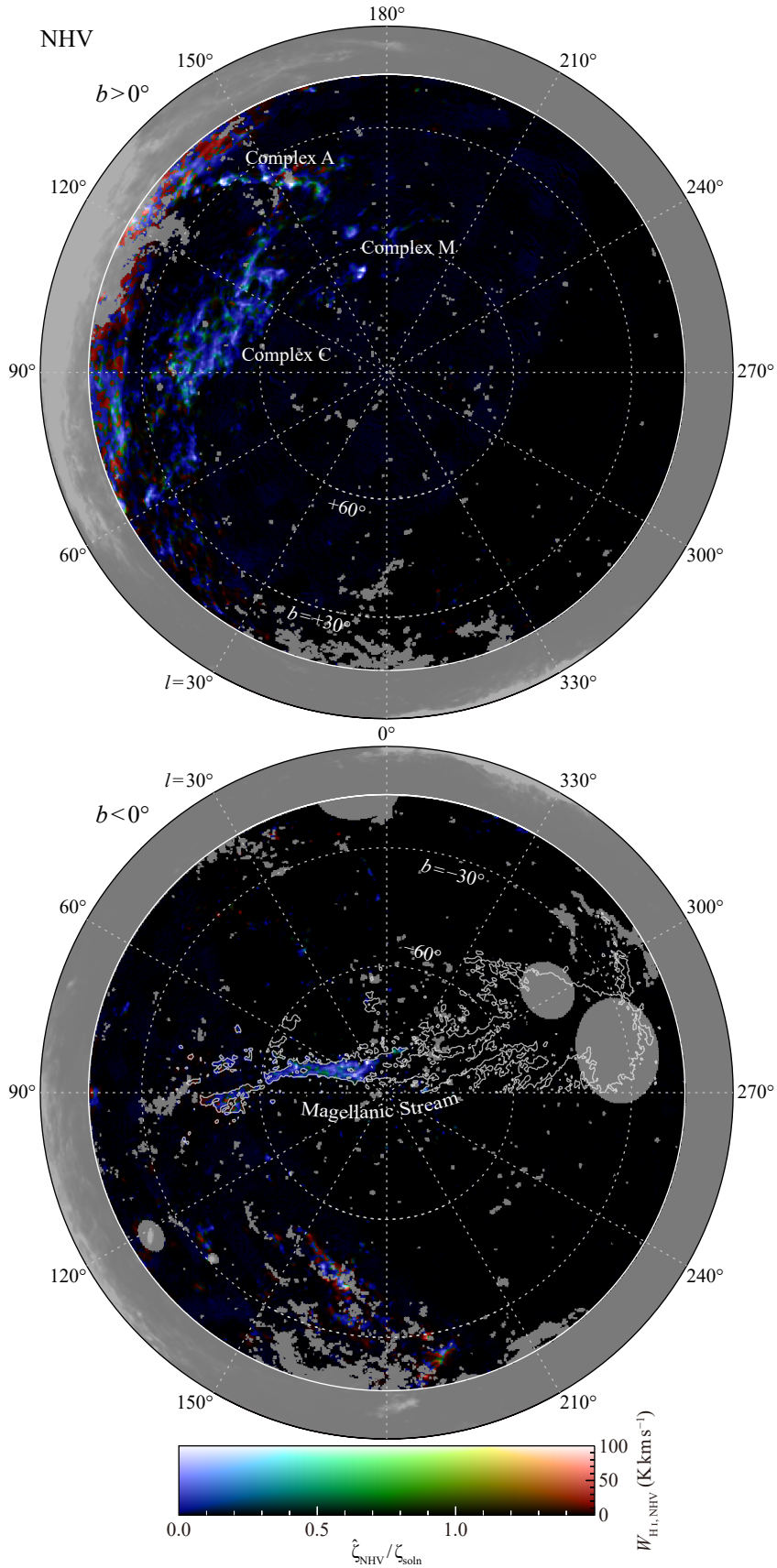


Figure 9 – continued (b) Same as (a) but for the NHV.

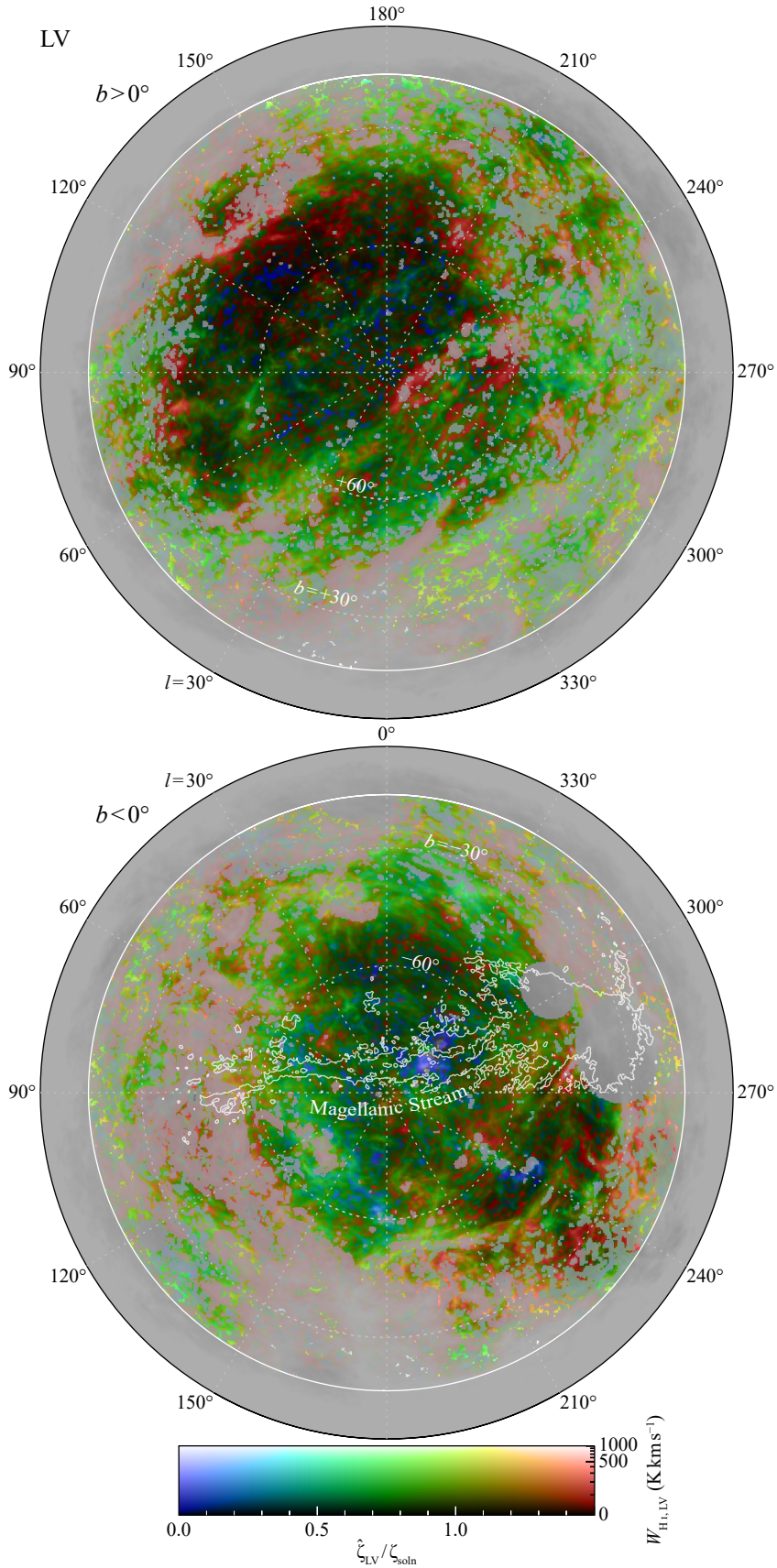


Figure 9 – continued (c) Same as (a) but for the LV.

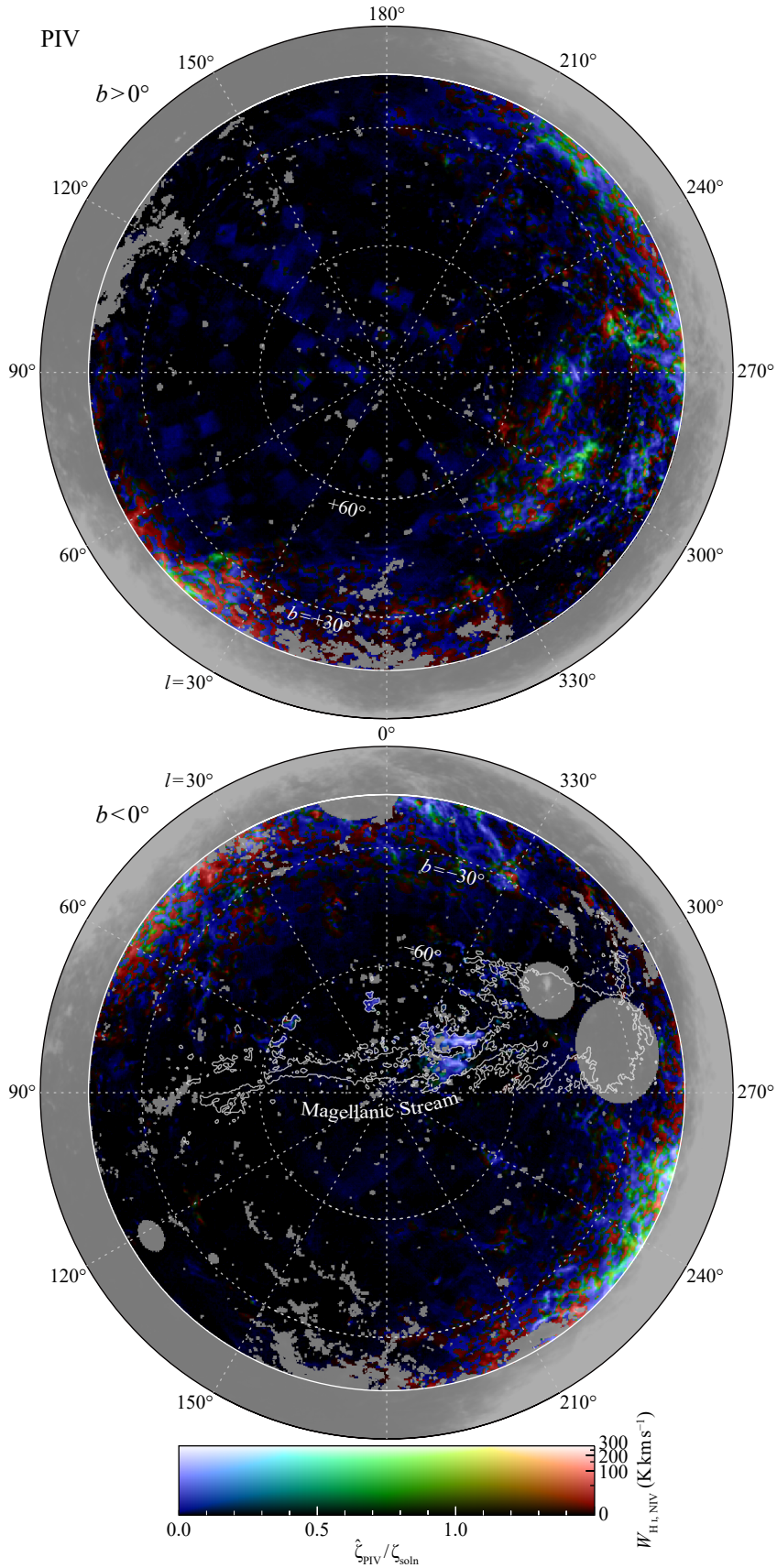


Figure 9 – continued (d) Same as (a) but for the PIV.

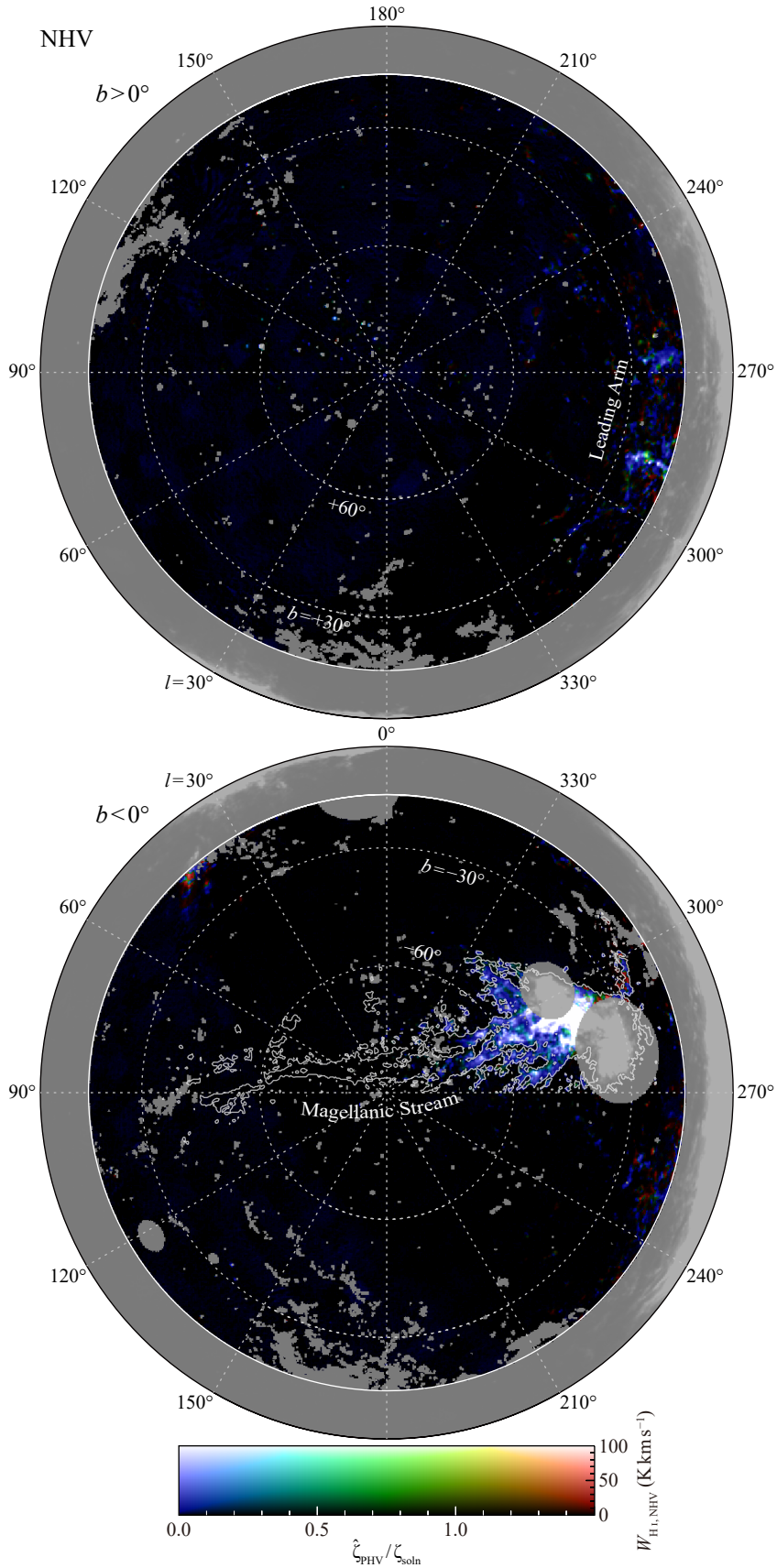


Figure 9 – *continued* (e) Same as (a) but for the PHV.

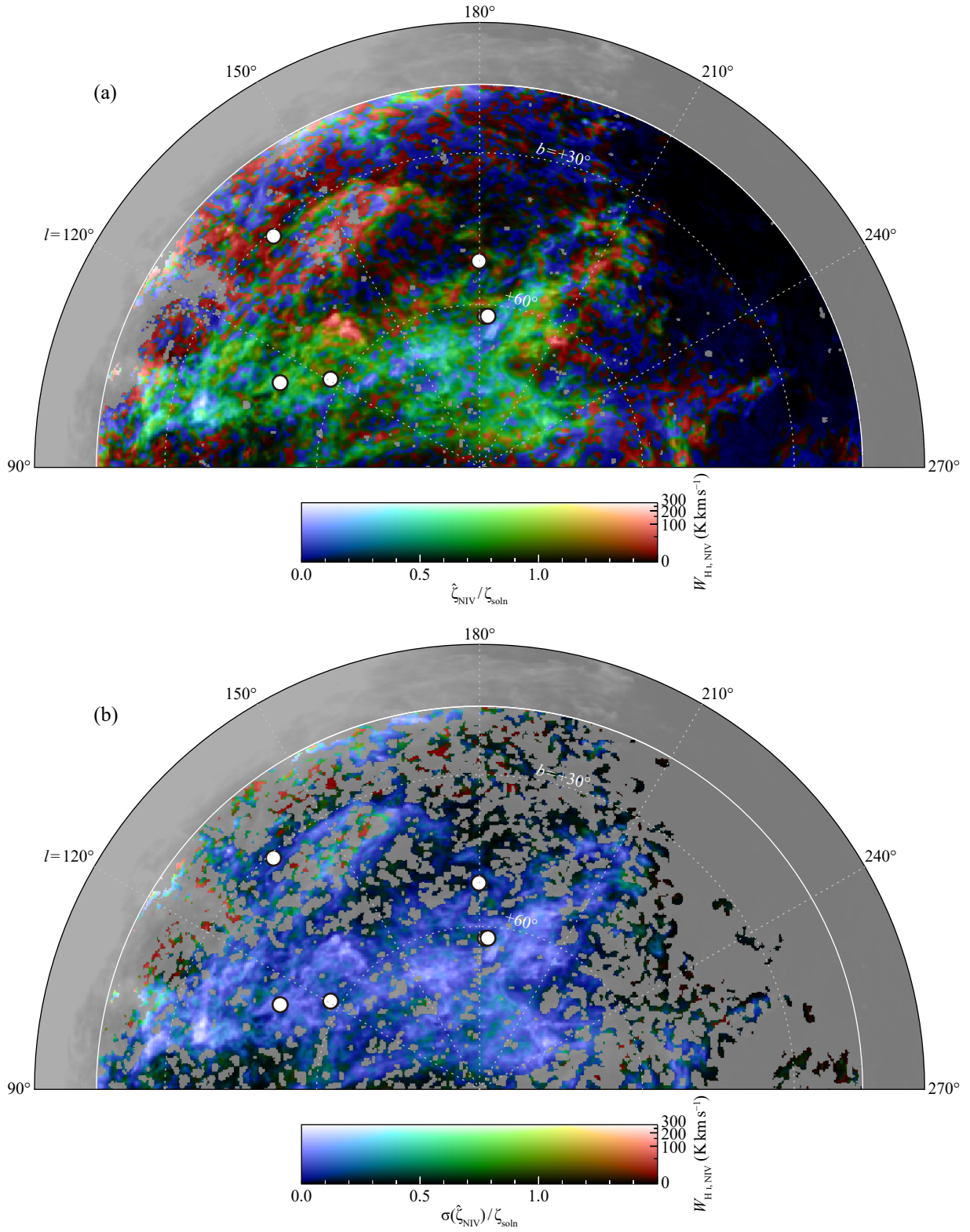


Figure 10. (a) A close up view of Fig. 9(a) focusing on the NIV-GN region containing IV Arch/Spur, LL IV Arch, and Complex M. (b) Same as (a) but the colour hue shows the standard error $\sigma(\hat{\zeta}_{\text{NIV}})/\zeta_{\text{soln}}$. The filled circles indicate the positions of the background objects where absorption measurements were made (see Table 2). The grey shadow presents the areas with no valid $\hat{\zeta}_{\text{NIV}}$ or $\sigma(\hat{\zeta}_{\text{NIV}})$ values.

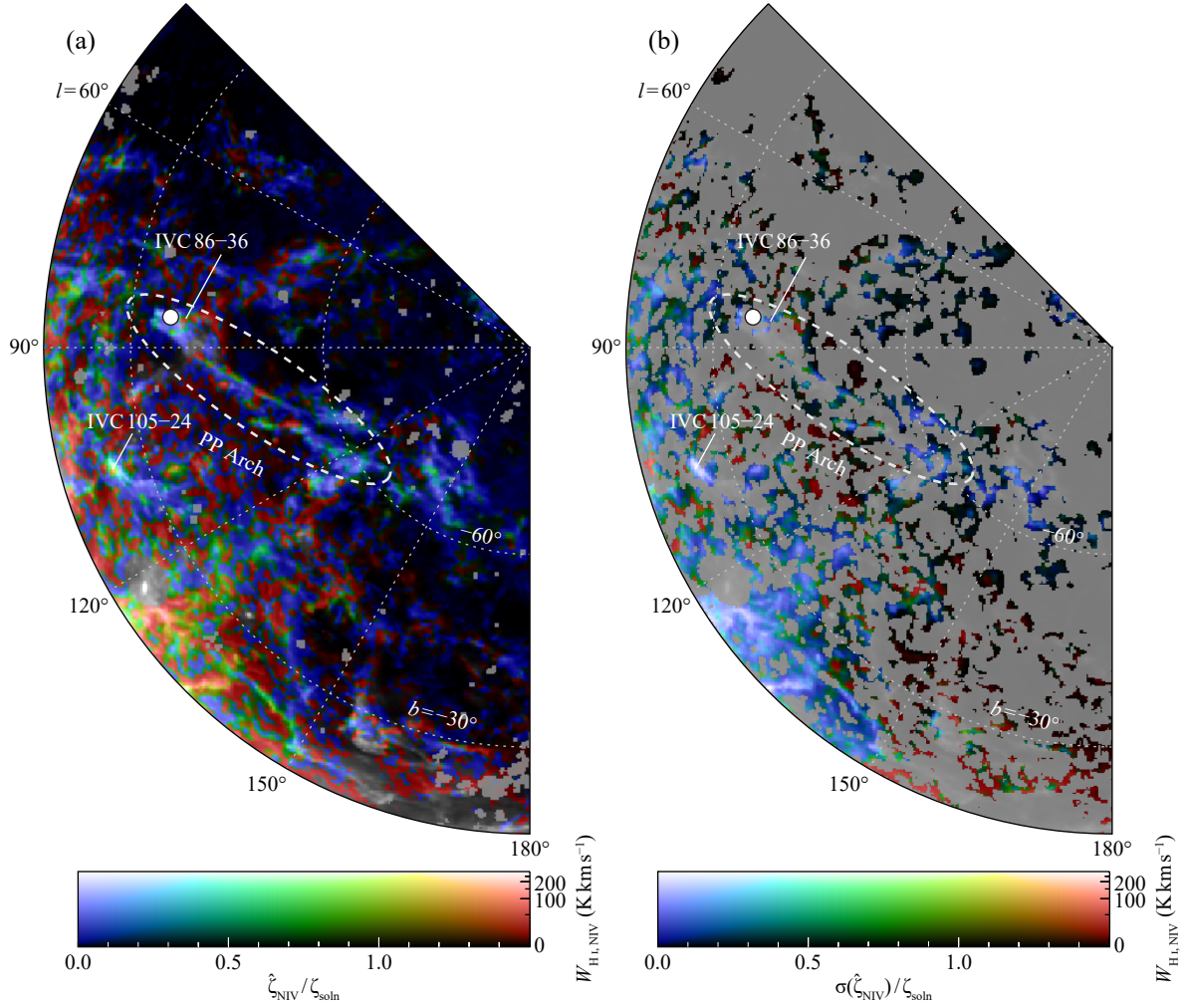


Figure 11. Same as Figure 10 but focusing on the NIV-GS region including PP Arch.

4.3 Regression analysis and results

We estimated $\zeta(l_i, b_i)$ at each pixel using the GWR technique. We used a truncated-Gaussian weighting function⁶

$$w_i(l_j, b_j) = \begin{cases} \exp\left[-\frac{1}{2}\left(\frac{\theta_{ij}}{\theta_{\text{bw}}}\right)^2\right] & (\theta_{ij} \leq \theta_{\text{tr}}) \\ 0 & (\text{otherwise}) \end{cases}, \quad (9)$$

where θ_{ij} is the great-circle angular distance between the regression point and the j -th ($j = 1, \dots, n$) pixel (l_j, b_j) , θ_{bw} is the bandwidth of the weighting function, and θ_{tr} is the truncation radius. We used $\theta_{\text{bw}} = 20$ arcmin (FWHM = 47 arcmin), and $\theta_{\text{tr}} = 1.2$ degree (truncates below $w_i(l_j, b_j) = 1 \times 10^{-3}$). The ζ cannot take negative values; negative ζ does not make physical sense and will overestimate the other coefficients. We thus introduced a non-negative least-squares (NNLS) regression technique. In the case either or both of the dust-to-H I ratio and the column density of the component X is

⁶ It is known empirically that the results of GWR are relatively insensitive to the choice of weighting function (e.g., Fotheringham et al. 2002). Not only Gaussian but also, for example, bi-square functions are often used.

meagre at a regression point, i.e., $\hat{\tau}_{353, \text{H I}, X} = (\hat{\zeta}_X C_0 W_{\text{H I}, X})^{\alpha 7}$ is roughly to say on the order of 10^{-8} or less, ζ_X is force set to 0 by using the algorithm of Lawson & Hanson (1995) (see their section 2 of chapter 23, also briefly summarised in Appendix B1 of the present paper) and treated as having no valid standard error value. The procedures and formulae in the regression analysis are summarised in Appendix B.

Although the regression model in equation (8) assumes optically-thin H I emission, saturation due to the optical-depth effects has been observed even in $|b| > 15^\circ$ skies (F15). The regression coefficients in saturation cases do not accurately represent the dust-to-H I ratio; therefore, we excluded them from the subsequent analysis using a simple judgment method. Fig. 8 shows the τ_{353} - $W_{\text{H I}, \text{LV}}$ correlations for optically thin (not saturated) and saturated examples. The best-fit line for the latter takes a large constant term (or intercept), whereas the one for the former throughs near the origin. We determined that H I emission toward a direction is saturated if the estimated value of the constant term $|\hat{\tau}_{353, 0}|$ exceeds 1×10^{-6} (1σ of all analysed pixels).

⁷ Throughout this study, the symbols with hat ($\hat{\quad}$) are estimates from regressions.

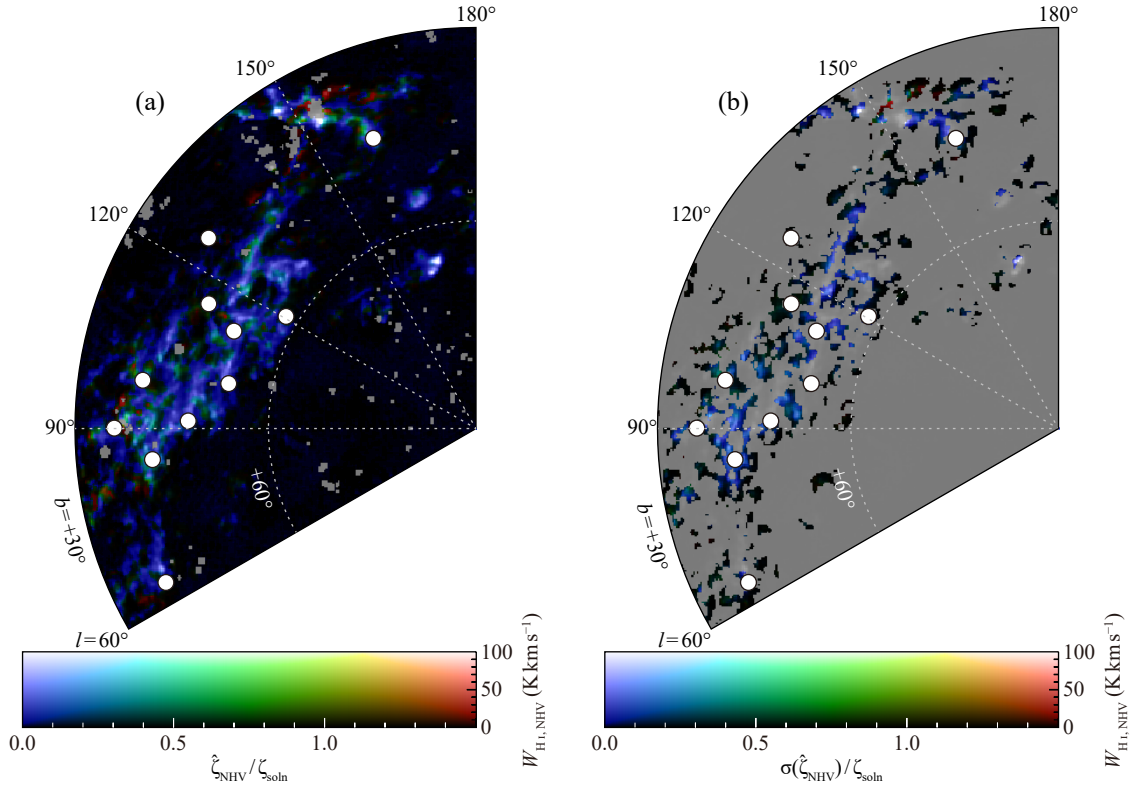


Figure 12. (a) A close up view of Fig. 9(b) focusing on the NHV-GN region including Complexes A/C/M. (b) Same as (a) but the colour hue shows the standard error $\sigma(\widehat{\zeta}_{\text{NHV}})/\zeta_{\text{soln}}$. The filled circles indicate the positions of the background objects where absorption measurements were made (see Table 2). The grey shadow presents the areas with no valid $\widehat{\zeta}_{\text{NHV}}$ or $\sigma(\widehat{\zeta}_{\text{NHV}})$ values.

Fig. 7 shows the saturated H I area. Note that saturation should not be an issue for the IVCs and HVCs due to their low column densities. This procedure was applied only to the LV component.

Fig. 9 shows the spatial distribution of estimated $\widehat{\zeta}/\zeta_{\text{soln}}$, where the solar neighbourhood dust-to-H I ratio $\zeta_{\text{soln}} = 6.29 \times 10^{-26} \text{ cm}^2$ is an empirical constant determined so that the LV component has a mode value of $\widehat{\zeta}_{\text{LV}}/\zeta_{\text{soln}} = 1.0$ and $\widehat{\zeta}/\zeta_{\text{soln}}$ present the ratios relative to the solar-neighbourhood value. Figs. 10–13 show close-up views of $\widehat{\zeta}/\zeta_{\text{soln}}$ and their standard error $\sigma(\widehat{\zeta})/\zeta_{\text{soln}}$ focusing on four regions-of-interest (ROIs), NIV-Galactic North (GN), NIV-Galactic South (GS), NHV-GN, and the Magellanic Stream (MS). Fig. 14 shows the distribution functions of $\widehat{\zeta}/\zeta_{\text{soln}}$ and $\sigma(\widehat{\zeta})/\zeta_{\text{soln}}$ in the LV and the four ROIs for all the pixels with valid values and also the fraction determined with $\sigma(\widehat{\zeta})/\zeta_{\text{soln}}$ better than 0.1. We find that in the IVCs and HVCs in the ROIs, the fraction with significant determination is ~ 50 per cent. This fraction is significantly larger than the previous results when the coverage in the sky is considered, particularly in terms of the solid angle. We give a detailed description of the individuals in the following subsection.

4.4 Description of the individuals

4.4.1 The LV component

Fig. 14(a) shows the distribution function of $\widehat{\zeta}_{\text{LV}}/\zeta_{\text{soln}}$. The ratio is determined in most pixels with a sufficiently high confidence level better than $\sigma(\widehat{\zeta}_{\text{LV}})/\zeta_{\text{soln}} = 0.1$. The peak of the distribution is normalised to 1.0 as intended, and a Gaussian function well approx-

imates the distribution. The measurements of the metallicity of G dwarfs were made for the local volume within 25 pc by many authors in the last five decades (e.g., Rocha-Pinto & Maciel 1996). These works indicate that the dispersion of metallicity is 0.2–0.3 dex with a peak at -0.2 dex. The dispersion is somewhat larger than the present one. Considering the much longer age of G dwarfs, several Gyr, than the dynamical timescale of H I gas, $\sim \text{Myr}$, the difference seems reasonable, and the H I gas in the local volume seems to be well mixed probably by the turbulent motion.

4.4.2 The NIV-GN region

The NIV-GN region ($l = 90^\circ\text{--}270^\circ$, $b > 15^\circ$) contains a large apparent amount of IVC in the complexes IV Arc/Spur, LL IV Arch and Complex M (Complex M straddles the -100 km s^{-1} boundary, part of which is in the NHV range in the present study).

The $\widehat{\zeta}_{\text{NIV}}/\zeta_{\text{soln}}$ in this region is peaked at 0.6 with a broad continuous shape ranging from less than 0.1 to high values beyond 1.5 (Fig. 14(b)). The absorption measurements toward bright background objects indicated the metallicity is near solar (see Table 2), i.e., not much different from the LV components. The present dust-to-H I ratio distribution gives a significantly different trend; there exists a significant amount of gas having $\widehat{\zeta}_{\text{NIV}}/\zeta_{\text{soln}} < 0.5$ (of the fractions with significance better than the $\sigma(\widehat{\zeta}_{\text{NIV}})/\zeta_{\text{soln}} = 0.1$ threshold, 10 per cent display $\widehat{\zeta}_{\text{NIV}}/\zeta_{\text{soln}} < 0.3$ and 20 per cent $\widehat{\zeta}_{\text{NIV}}/\zeta_{\text{soln}} < 0.5$). This difference is likely caused by the tiny fraction of the IVCs observed by the absorption measurements.

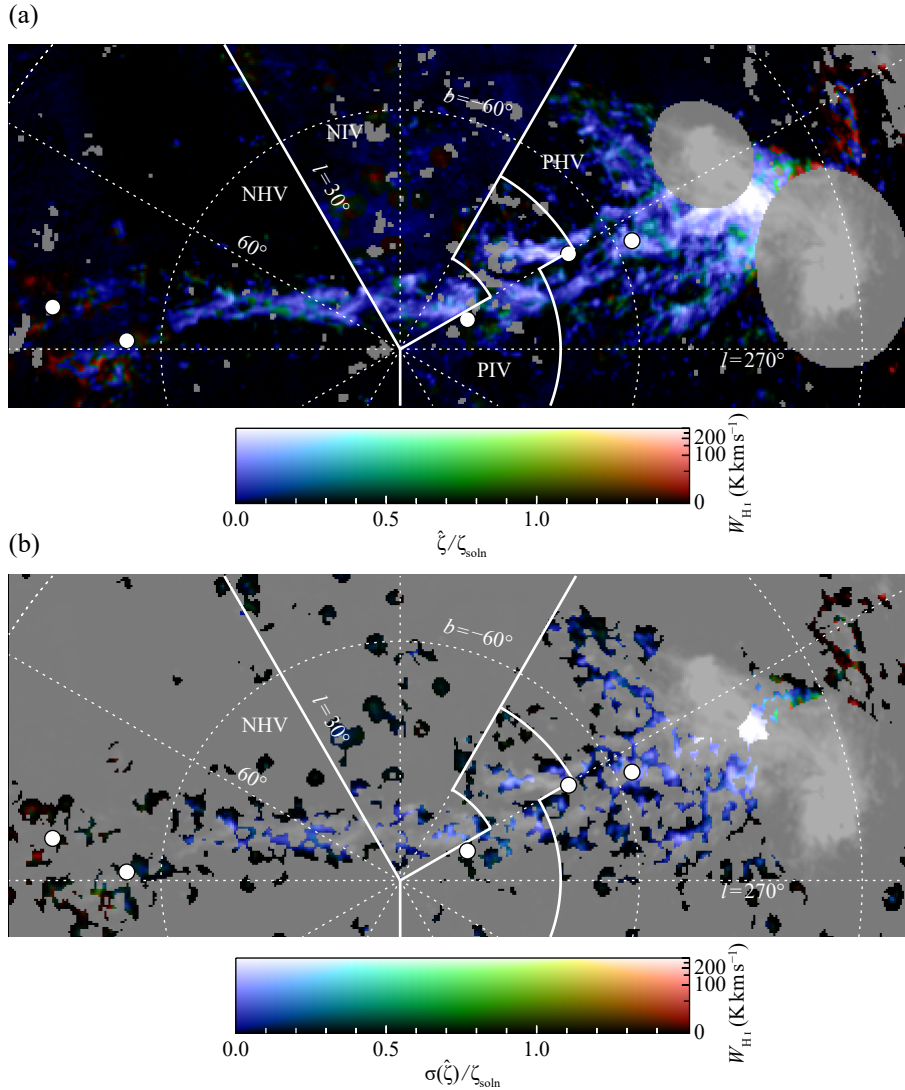


Figure 13. (a) A patchwork of the NHV, NIV, PIV, and PHV maps showing the spatial distribution of the dust-to-H I ratio $\widehat{\zeta}/\zeta_{\text{soln}}$ (colour) and $W_{\text{H I}}$ (brightness) in the Magellanic Stream. (b) Same as (a) but the colour hue shows the standard error $\sigma(\widehat{\zeta})/\zeta_{\text{soln}}$. The filled circles indicate the positions of the background objects where absorption measurements were made (see Table 2). The grey shadow presents the areas with no valid $\widehat{\zeta}$ or $\sigma(\widehat{\zeta})$ values.

4.4.3 The NIV-GS region

The most prominent object in the NIV-GS region ($l = 45^\circ\text{--}180^\circ$, $b > 15^\circ$) is PP Arch. The present result reveals that the head of PP Arch (IVC 86–36) has a low $\widehat{\zeta}_{\text{NIV}}/\zeta_{\text{soln}}$ distribution peaked at $\sim 0.2\text{--}0.3$, consistent with the (F21) results, and the tail exhibits even lower values. Another head-tail structure IVC elongated from $(l, b) = (105^\circ, -24^\circ)$ parallel to PP Arch (referred to as IVC 105–24 for convenience) shows similar $\widehat{\zeta}_{\text{NIV}}/\zeta_{\text{soln}}$ values, suggesting that they are the same type of object. Many other unidentified minor IVCs are in low latitudes, some of which appear to be connected to the Galactic disc. The $\widehat{\zeta}_{\text{NIV}}/\zeta_{\text{soln}}$ values in the NIV-GS region exhibit a gently flat distribution ranging from 0.1 or below to 1.5 and above (Fig. 14(c)).

4.4.4 The NHV-GN region

The NHV-GN region ($l = 60^\circ\text{--}180^\circ$, $b > 30^\circ$) focuses on Complex C as well as Complexes A and M. Complex C has the largest apparent

size among HVC complexes in $|b| > 15^\circ$ skies outside the Magellanic Stream.

There have been several attempts to detect thermal dust emission associated with HVCs (e.g., Wakker & Boulanger 1986; Saul et al. 2014), some possible detections (e.g., Peek et al. 2009; Lenz et al. 2016), but no confident one have been reported⁸. The difficulty is due to the low column density and the low metallicity. In the present work, barely sufficient column density in the scattered small areas allows the dust-to-H I estimation (Fig. 12). Fig. 14(d) indicates that $\widehat{\zeta}_{\text{NHV}}/\zeta_{\text{soln}}$ in this region peaked at 0.1–0.2 with a relative uncertainty of $\sigma(\widehat{\zeta}_{\text{NHV}})/\widehat{\zeta}_{\text{NHV}} \sim 1$ and is even lower than $\widehat{\zeta}_{\text{NIV}}/\zeta_{\text{soln}}$ in the NIV-GN region (Fig. 14(b)). More than 50 per cent of the fractions with $\sigma(\widehat{\zeta}_{\text{NHV}})/\zeta_{\text{soln}} < 0.1$ exhibit $\widehat{\zeta}_{\text{NHV}} < 0.3$, indicating the low dust content in the HVC.

⁸ [Miville-Deschênes et al. 2005](#) claims the first detection, but this is controversial, as argued by [Peek et al. \(2009\)](#).

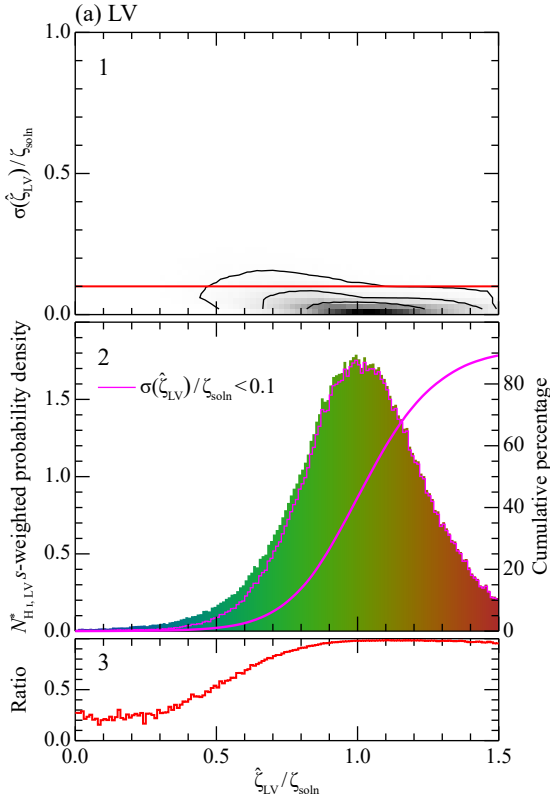


Figure 14. (a)-1 Density plot showing the two-dimensional probability density with respect to $\hat{\zeta}_{LV}/\zeta_{soln}$ (horizontal axis) and its standard error $\sigma(\hat{\zeta}_{LV})/\zeta_{soln}$ (vertical axis) for the LV component, weighted by the apparent amount of H I gas $N_{H I, LV}^*$ of each pixel. The contours contain 50, 75, and 90 per cent of the total amount. The horizontal line indicates $\sigma(\hat{\zeta}_{LV})/\zeta_{soln} = 0.1$. (a)-2 The filled histogram shows (i) a projection of the above onto the horizontal axis, and the solid line histogram shows (ii) the subset better than $\sigma(\hat{\zeta}_{LV})/\zeta_{soln} = 0.1$. The overlaid curves depict the cumulative percentage of (ii) (the scale is displayed on the right-hand vertical axis). (a)-3 The ratio of (ii) to (i).

4.4.5 The Magellanic Stream

The Magellanic Stream is a well-known giant filamentous structure, starting at the Magellanic Clouds and trailing over 100 degrees, having a large velocity gradient from $+180 \text{ km s}^{-1}$ near the Clouds to -450 km s^{-1} at the tip. Fig. 13 is a patchwork of the NHV, NIV, PIV, and PHV maps showing the spatial distribution of $\hat{\zeta}/\zeta_{soln}$ and Fig. 14(e) shows the distribution function. The MS has the lowest dust-to-H I ratio among the four ROIs, with a mode at ~ 0.1 and a tail extending to ~ 0.5 .

5 DISCUSSION

5.1 Comparison of the present dust-to-H I ratio with the absorption-line measured metallicity

The present work revealed the dust-to-H I ratio distribution which covers a large fraction of the ISM, the IVCs, and the HVCs. Dust only traces solid-phase heavy elements but is often, and also in the present study, used as a proxy for the gas-phase heavy elements assuming a nearly constant dust-to-metal (DTM) ratio. Recent studies of nearby galaxies show that well-evolved galaxies with metallicities $12 + \log(\text{O}/\text{H}) \gtrsim 8.2$ (cf. the solar value is 8.7, e.g., Asplund et al.

2009) have a more or less constant DTM ratio (e.g., De Vis et al. 2019). In the context of the low-velocity gas of the solar neighbourhood, these results support the assumption that the DTM ratio is constant and that the dust-to-H I ratio is a good proxy for metallicity.

We demonstrate in Fig. 15 that the present estimates are not far from the previous absorption-line measurements in Table 2, whereas the discrepancies toward PG 0804+761 (LL IV Arch), RX J2043.1+0324 (the Smith Cloud) and Fairall 9 (the MS) suggest potential variations in the DTM ratio. Based on the current limited observational data, it is hard to evaluate how generally the abovementioned assumption holds for IVCs and HVCs.

5.2 Impact of the dust associated with the warm ionized medium on the estimates of the dust-to-H I ratio

The diffuse warm ionized medium (WIM) outside of localized H II regions is another significant component of the ISM. The absorption-line studies revealed that HVCs and IVCs are associated with the ionized components (e.g., Sembach et al. 2003; Shull et al. 2009; Lehner & Howk 2011). The velocity-resolved high-sensitivity surveys of diffuse H α emission using Wisconsin H α Mapper (WHAM) showed that the neutral and ionized components trace each other well, though the detailed structure is not identical (e.g., Tufte et al. 1998; Haffner et al. 2001; Barger et al. 2012, 2017). The estimated mass of the associated ionized component is roughly comparable to that of the neutral counterpart.

The observational evidence for the WIM-related dust is reported (Howk & Savage 1999; Dobler et al. 2009; Werk et al. 2019), but the extent to which it contributes to the FIR/submillimeter optical depth is poorly understood. Previous works attempted to decompose the dust emission intensity into the WIM-related and H I-related components. Lagache et al. (1999, 2000) claimed that they made a decomposition for the first time and that the FIR dust emissivity associated with WIM is close to the one with H I. On the contrary, Odegard et al. (2007) reported that the WIM-related component is consistent with zero within the uncertainties. Casandjian et al. (2022) reported that the FIR emission of the dust associated with a Reynolds layer of ionized hydrogen is below their detection limit. These authors used regression models expressing dust emission intensity as a linear combination of $N_{H I}$ and H α emission intensity ($I_{H\alpha}$). We performed an alternative analysis by taking another approach.

In Section 4, we estimated the dust-to-H I ratio ζ by making a least-squares fit to the regression model of equation (8). We refer to this as the “without-WIM-terms model” in this section and set up another “with-WIM-terms model”

$$\begin{aligned} \tau_{353}(l_i, b_i) = & \tau_{353,0}(l_i, b_i) + C_0^\alpha \sum_X [\zeta_X(l_i, b_i) W_{H I, X}(l_i, b_i)]^\alpha \\ & + \sum_X \tau_{353, H^+, X}(l_i, b_i). \end{aligned} \quad (10)$$

under the assumption that there is some contribution to τ_{353} from the dust associated with the WIM ($\tau_{353, H^+, X}$). The dust optical depth is a function of column density, whereas $I_{H\alpha}$ is the line-of-sight integral of the electron temperature T_e , density n_e and ionized hydrogen density n_{H^+}

$$I_{H\alpha} = \frac{1}{2.75} \int \left(\frac{T_e}{10^4 \text{ K}} \right)^{-0.924} n_e n_{H^+} dl, \quad (11)$$

where dl is the line-of-sight path length over which the electrons are recombining. The distribution of T_e and $n_e \approx n_{H^+}$ in a line of sight is

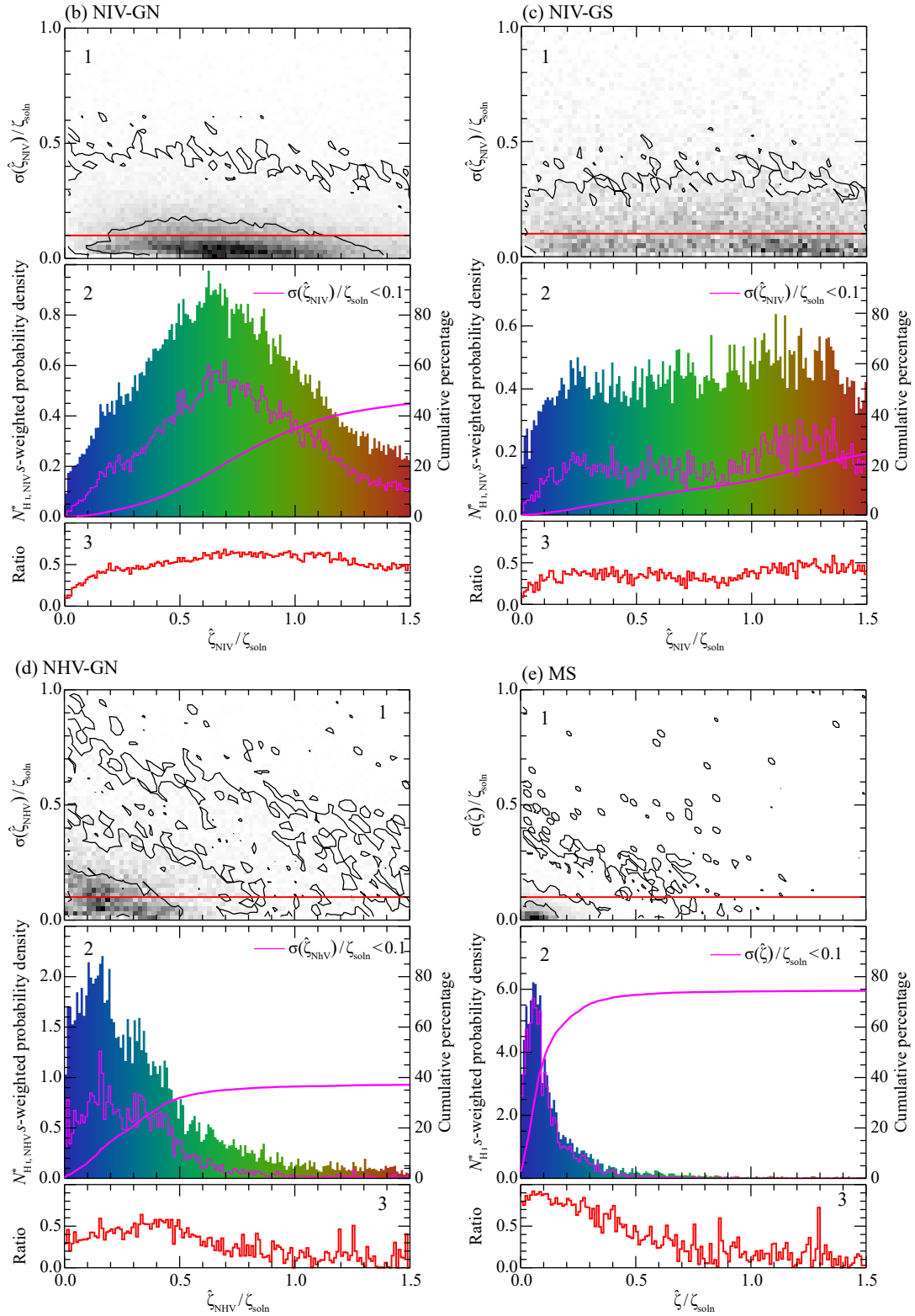


Figure 14 – *continued* Same as (a) but for (b) the NIV-GN, (c) NIV-GS, (d) NHV-GN, and (e) MS regions.

Table 2. List of the absorption measurements.

		Absorption Measurements						
	Background ^a	Position ^b		Ion	V_{LSR}^c (km s^{-1})	A/A_{\odot}^d	Ref. ^e	$\hat{\zeta}/\zeta_{\text{soln}}^f$
		l	b					
Complex A	I Zw 18	160°53	+44°84	O I	-160	0.062	1, 2	0
Complex C	Mrk 501	63°60	+38°86	O I	-135--65	< 0.29	3	0
	PG 1626+554	84°51	+42°19	O I	-155--75	$0.16^{+0.04}_{-0.04}$ - $0.39^{+0.21}_{-0.18}$	4	0.1 ± 0.1
	3C 351	90°08	+36°38	O I	-128	$0.17^{+0.09}_{-0.08}$ ^g	5	0.08 ± 0.61
						$0.12^{+0.02}_{-0.02}$ - $0.21^{+0.08}_{-0.04}$	4	
	Mrk 290	91°49	+47°95	O I	-165--75	$0.09^{+0.06}_{-0.03}$	4	0.02 ± 0.21
	Mrk 876	98°27	+40°38	O I	-135	$0.20^{+0.08}_{-0.07}$	4	0
					-175	$0.26^{+0.13}_{-0.17}$		
	Mrk 817	100°30	+53°48	O I	-140--80	$0.29^{+0.17}_{-0.06}$	3, 4	0.2 ± 0.1
					-148.6, -113.8, -86.0	$0.33^{+0.21}_{-0.17}$ ^g	6	
	PG 1351+640	111°89	+52°02	O I	-190--95	< 0.38	3, 4	0
	Mrk 279	115°04	+46°86	O I	-200--120	$0.11^{+0.04}_{-0.03}$	4	0.5 ± 0.6
	PG 1259+593	120°56	+58°05	O I	-130	$0.093^{+0.123}_{-0.047}$	7	0.31 ± 0.04
				O I	-155--95	$0.10^{+0.05}_{-0.04}$	3, 4	
			O I	-129.5, -112.5	$0.16^{+0.04}_{-0.06}$	8		
Mrk 205	125°45	+41°67	O I	-165--125	$0.17^{+0.05}_{-0.05}$	4	0	
Smith Cloud	RX J2043.1+0324	49°72	-22°88	S II	+58.5	$0.72 \pm 0.22 \pm 0.25^g$	9	1.9 ± 0.1
	PG 2112+059	57°04	-28°01		+41.5	$0.81 \pm 0.62 \pm 0.28^g$		0
	RX J2139.7+0246	58°09	-35°01		+53.7	$0.26 \pm 0.12 \pm 0.09^g$		0
Complex WE	HD 156359	328°68	-14°52	O I	+125.0	2.3 ± 0.6	10	...
Complex K	3C 351	90°08	+36°38	O I	-82	> 0.30 ^g	5	0.7 ± 0.6
Cloud MIII	BD +38°2182	182°16	+62°21	O I	-85	> 0.27	2, 11	0.6 ± 0.3
IV Arch	HD 121800	113°01	+49°76	S II	-69	0.78	2	0.84 ± 0.03
					-37	0.81		
	PG 1259+593	120°56	+58°05	O I	-55	$0.98^{+1.21}_{-0.46}$	7	1.1 ± 0.1
					-81.9, -54.5, -29.0	0.79 ± 0.18	8	
	PG 0953+414	179°79	+51°71	S II	-40	1.1	2	1.4 ± 0.1
	HD 93521	183°14	+62°15	S II	-66.3	2.1	2, 12	1.1 ± 0.2
					-57.7	0.78		
				-51.2	1.2			
				-38.8	0.74			
				...	1.0 ^h			
LLIV Arch	PG 0804+761	138°28	+31°03	O I	-55	1.0	2	2.1 ± 0.1
PP Arch	HD 215733	85°16	-36°35	S II	-93	0.17	2, 13	0
					-56	0.32		
					-43	1.2		
MS	NGC 7469	83°10	-45°47	O I	-335	$0.10 \pm 0.01 \pm 0.02$	14	0
	NGC 7714	88°22	-55°56	O I	-320	0.06 ± 0.03	15	0
	HE 0056-3622	293°72	-80°90	O I	+150	0.09 ± 0.04	15	0
	Fairall 9	295°07	-57°83	S II	+125--250	$0.28 \pm 0.04^{+0.11}_{-0.14}$	16	0.06 ± 0.01
					+143--218	0.50 ± 0.05	17	
RBS 144	299°48	-65°84	S II	+92	0.07 ± 0.03	15	0	

^a Name of the background object

^b Galactic coordinates of the background object

^c LSR velocity of the absorption line

^d Ion abundance relative to the solar value

^e References — 1 Kunth et al. (1994), 2 Wakker (2001), 3 Collins et al. (2003), 4 Collins et al. (2007), 5 Tripp et al. (2003), 6 Fox et al. (2023), 7 Richter et al. (2001b), 8 Sembach et al. (2004), 9 Fox et al. (2016), 10 Cashman et al. (2023), 11 Danly et al. (1993), 12 Spitzer & Fitzpatrick (1993), 13 Fitzpatrick & Spitzer (1997), 14 Fox et al. (2010), 15 Fox et al. (2013), 16 Gibson et al. (2000), 17 Richter et al. (2013)

^f Estimated dust-to-H I ratio relative to the solar-neighbourhood value, toward the nearest neighbour of the background object (this work)

^g With ionization correction

^h The average of the -66.3, -57.7, -51.2, and -38.8 km s^{-1} components, based on H I column density

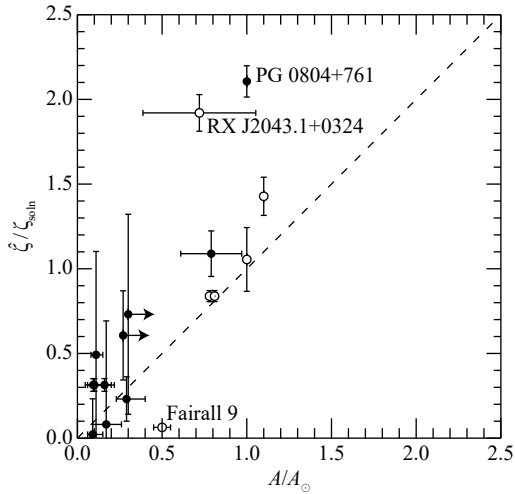


Figure 15. The correlation between the ion abundances A/A_{\odot} obtained by absorption measurements (see Table 2) and $\widehat{\zeta}/\zeta_{\text{soln}}$ (this work). The dashed line shows the line where both have the same value. The filled and open symbols represent that the A/A_{\odot} correspond to measurements from O I and S II observations, respectively. The arrows attached to the filled circles indicate that the A/A_{\odot} values are the lower limit.

usually unknown. Assuming that they are constant over the emitting region, we can approximate equation (11) as

$$I_{\text{H}\alpha} \propto n_{\text{H}^+}^2 L, \quad (12)$$

and N_{H^+} is given as

$$N_{\text{H}^+} \simeq n_{\text{H}^+} L \propto (LI_{\text{H}\alpha})^{1/2}, \quad (13)$$

where $L = \int dl$. Then, we assume that the WIM term is proportional to $I_{\text{H}\alpha}^{1/2}$. The WHAM Sky Survey (Haffner et al. 2003, 2010) is the sole velocity-resolved all-sky H α survey data presently available but provides us with no information on the high-velocity ($|V_{\text{LSR}}| \gtrsim 100 \text{ km s}^{-1}$) WIM. If $\tau_{353, \text{H}^+, \text{NHV}}$ and $\tau_{353, \text{H}^+, \text{PHV}}$ are tiny fraction, close to $\widehat{\tau}_{353, \text{H}^+, \text{NHV}}$ and $\widehat{\tau}_{353, \text{H}^+, \text{PHV}}$ (on the order of 10^{-8} or less), then approximating them to 0 would not significantly affect the results. In summary, the WIM term is given as

$$\tau_{353, \text{H}^+, X}(l_i, b_i) = \begin{cases} 0 & X = \text{NHV}, \text{PHV} \\ \eta_X(l_i, b_i) [I_{\text{H}\alpha, X}(l_i, b_i)]^{1/2} & \text{otherwise} \end{cases} \quad (14)$$

We emphasize that the coefficients η_X in the WIM terms are not dust-to-WIM ratios, unlike the coefficients ζ_X in the H I terms. Using $I_{\text{H}\alpha}$ instead of $(I_{\text{H}\alpha})^{1/2}$ almost reproduces the same results described below, indicating that the reality of the WIM terms in the model is not a very important issue in this discussion.

Fig. 16, the H α intensity ($I_{\text{H}\alpha}$) maps in the NIV, LV, and PIV velocity ranges, shows that the data suffer from zero-level offsets (typically $\sim 0.1\text{--}0.2 \text{ R}$, where $1 \text{ R} = 10^6/4\pi \text{ photons cm}^{-2} \text{ s}^{-1} \text{ sr}^{-1}$) and block discontinuity, probably due to data-reduction issues. We, therefore, used the data in $l = 90^\circ\text{--}150^\circ$ and $b > 45^\circ$ in the following analysis, where the WHAM data are of acceptable quality (judged by the eye), and the optically-thick LV H I occupies a small fraction of the area. The WHAM-SS is undersampled with a 1 deg beam at a 1 deg spacing (see Haffner et al. 2003, section 2.2), having a $\sim 3\text{--}12$ times lower resolution than the HI4PI and *Planck* data, and we convolved the $W_{\text{H}1}$ and τ_{353} data with the WHAM beam

centred on each WHAM pointing. Following Finkbeiner (2003), we approximated the WHAM beam to be a smoothed top-hat function

$$f(\theta) = \frac{1}{\exp[(\theta - \theta_0)/\theta_s] + 1}, \quad (15)$$

where θ is the angular distance from the beam center, θ_0 and θ_s are set to 0.5 and 0.025 deg, respectively.

Fig. 17(a) compares the estimates of $\widehat{\zeta}_{\text{NIV}}$ obtained using the “without-WIM-terms model” and those obtained using the “with-WIM-terms model”, and Fig. 17(b) compares $\widehat{\zeta}_{\text{LV}}$. The two models produce statistically similar results, although minor discrepancies exist in individual data points. Fig. 18 shows a clear tendency that the constant term $\tau_{353,0}$ in the “with-WIM-terms model” is somewhat smaller (note that this is only a comparison of the results from the two models and does not prove or measure $\tau_{353, \text{H}^+, X}$, as it is uncertain how realistic the WIM terms in the model are).

In multiple regression analysis, generally, the constant term represents the portion of the dependent variable (τ_{353} in the present study) which is not significantly correlated with the independent variable ($W_{\text{H}1, X}$ in the “without-WIM-terms model”). The contribution to τ_{353} from dust associated with WIM, if any, is included in the constant term in the “without-WIM-terms model” and has negligible impact on the estimates of ζ in the present study unless it is highly correlated with the H I spatial distribution on a scale of ~ 1 degree.

5.3 The dust-to-gas ratio of the H I components

The derived dust-to-H I ratio in the LV component and the four ROIs (Section 4) exhibits the following characteristics.

- (i) The ratio in the LV component has a distribution peaked at $\widehat{\zeta}_{\text{LV}}/\zeta_{\text{soln}} = 1.0$ with a Gaussian shape having dispersion somewhat smaller but similar to the metallicities of G dwarfs in the local volume.
- (ii) The NIV-GN region has a distribution with a significant fraction (25 per cent) of gas with a low ratio of $\widehat{\zeta}_{\text{NIV}}/\zeta_{\text{soln}} < 0.5$. In the NIV-GS region, PP Arch and IVC 105–24 exhibit a low $\widehat{\zeta}_{\text{NIV}}/\zeta_{\text{soln}} \lesssim 0.3$.
- (iii) The distribution in the NHV-GN peaked at $\widehat{\zeta}_{\text{NHV}}/\zeta_{\text{soln}} = 0.1\text{--}0.2$, and more than 50 per cent of the fraction have ratios $\widehat{\zeta}_{\text{NHV}}/\zeta_{\text{soln}} < 0.3$.
- (iv) The Magellanic Stream has the lowest distribution peaked at $\widehat{\zeta}/\zeta_{\text{soln}} < 0.1$ and more than 80 per cent of the fraction have ratios $\widehat{\zeta}/\zeta_{\text{soln}} < 0.2$.

We find that the LV, NHV-GN and the Magellanic Stream results are reasonably consistent with the previous absorption measurements, whereas the IVC results differ significantly from the previous results.

The conventional interpretation of the IVC is the Galactic fountain model, i.e., the stellar explosion in the plane feeds the high-metallicity gas to the Galactic halo to form the IVCs. We argue that the present results require a model that the extragalactic low metallicity gas also supplies a significant fraction of the IVCs. Otherwise, the significant fraction (20 per cent) of the gas with $\widehat{\zeta}_{\text{NIV}}/\zeta_{\text{soln}} < 0.3\text{--}0.5$ cannot be explained. Further, the interaction of the low metallicity IVCs with the high metallicity gas in the Galactic halo is an important mechanism to increase the metallicity in the IVCs. Gritton et al. (2017) and Henley et al. (2017) have recently discussed this possibility. It is very likely that the IVCs are dynamically interacting with the Galactic halo gas, as shown in IVC 86–36 by F21. The interaction causes deceleration of the IVCs along with the accretion and mixing with the halo gas. The interaction likely produces a trend that the metallicity, as well as the cloud mass, is increased along with the deceleration in the sense that the higher metallicity gas has a lower velocity. The

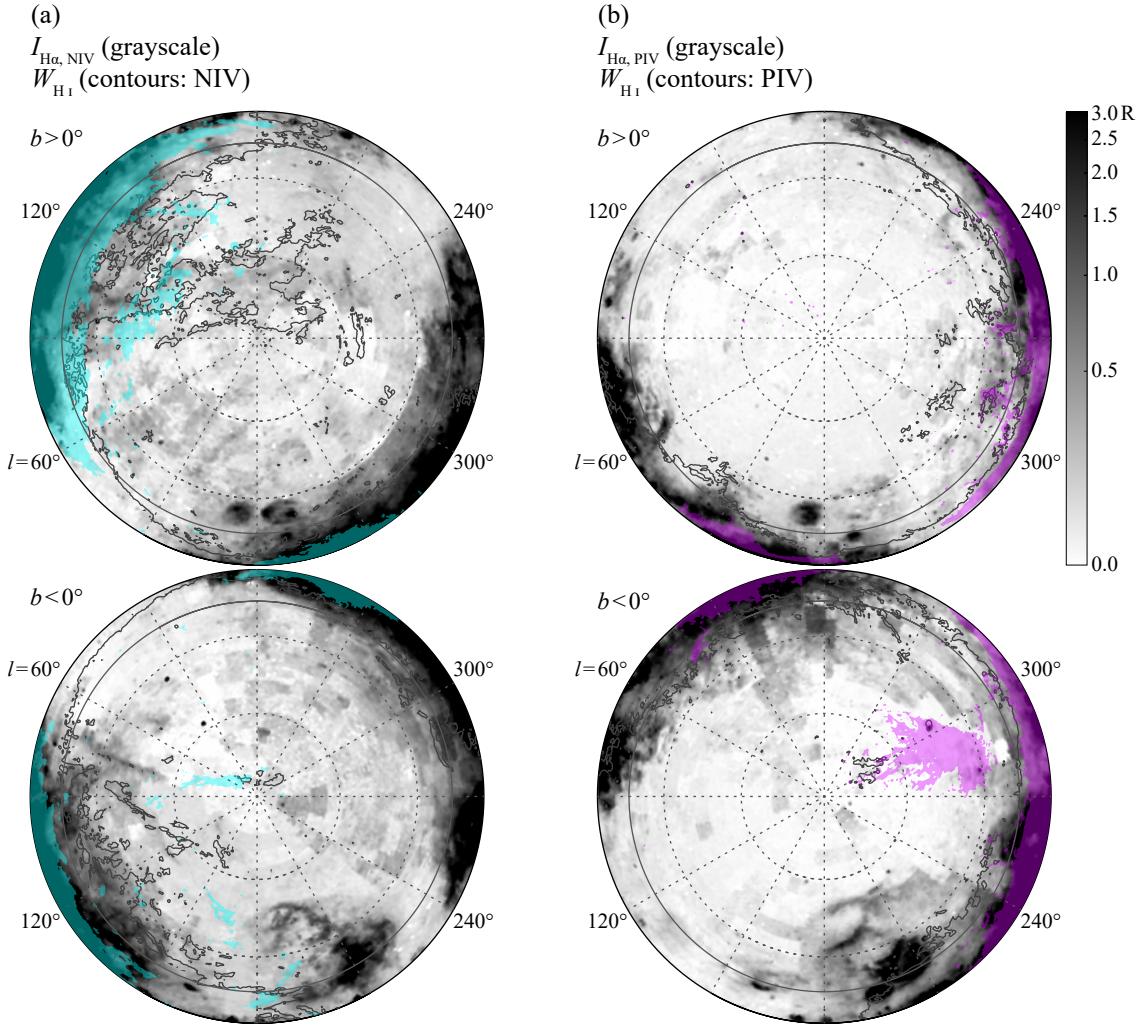


Figure 16. (a) The grayscale image shows the spatial distribution of $H\alpha$ intensity $I_{H\alpha}$ (Haffner et al. 2003, 2010) in the NIV velocity range shown in the same projection as Fig. 2. The southern limit of the WHAM northern sky survey (Haffner et al. 2003), $\delta_{J2000} = -30^\circ$, is presented by thick broken lines. The contours show $W_{H\text{I},\text{NIV}} = 30 \text{ K km s}^{-1}$ in the same velocity range, and the cyan silhouette shows the NHV $H\text{I}$ components with $W_{H\text{I},\text{PHV}} > 10 \text{ K km s}^{-1}$. The grey solid lines indicate $|b| = 15^\circ$. The circular sectors bounded by thick solid lines present the two regions analyzed in Section 5.2. (b) Same as (a) but for the PIV velocity range. The contours show $W_{H\text{I},\text{PIV}} = 30 \text{ K km s}^{-1}$ and the magenta silhouette shows the PHV $H\text{I}$ components with $W_{H\text{I},\text{PHV}} = 10 \text{ K km s}^{-1}$.

effect is approximately quantified as the mass increasing by a factor of two, accompanying a velocity decrease by a factor of two due to momentum conservation. Concerning the metallicity, the interaction between an infalling cloud with a metallicity of 0.2 and the halo gas with a metallicity of 1.0 having the same mass will result in a metallicity of 0.6, which is closer to the halo metallicity than the infalling cloud, when the two gases are fully mixed. The interaction has a strong impact on the observed metallicity of the IVCs.

6 CONCLUDING REMARKS

We conducted a multiple-regression analysis combining 21 cm $H\text{I}$ emission data with sub-mm dust optical depth τ_{353} to investigate the dust-to- $H\text{I}$ ratio in the $H\text{I}$ gas outside the Galactic plane. We have resulted in a comprehensive dust-to- $H\text{I}$ ratio distribution for the IVCs, HVCs, Magellanic Stream, and the low-velocity component in the solar neighbourhood at an effective resolution of 47 arcmin, which differs from the conventional optical absorption line measurements

toward bright galaxies and stars that cover a tiny fraction of the gas. The main conclusions are summarised below.

(i) The present study allowed us to derive the dust-to- $H\text{I}$ ratio over a far greater portion of the $H\text{I}$ gas than the previous studies. The major results include that the dust-to- $H\text{I}$ ratio of the IVCs (relative values to the solar-neighbourhood value) varies from < 0.2 to > 1.5 and that a significant fraction, 20 per cent, of the IVCs includes the dust-poor gas of < 0.5 with a mode at 0.6. In addition, it is shown that more than 50 per cent of the HVCs in Complex C have ratios of < 0.3 and that the Magellanic Stream has the lowest ratio with a mode at ~ 0.1 .

(ii) We argue that a large fraction of the dust-poor IVC indicates that the infalling external $H\text{I}$ gas of low metallicity is significant in the IVCs. A possible picture is that the low metallicity IVCs are falling onto the Galactic plane and are interacting with the high metallicity gas in the Galactic halo. Such interaction is evidenced by the kinematic bridge features connecting the IVCs with the disc as observed, for instance, in IVC 86–36 in PP Arch, and will cause

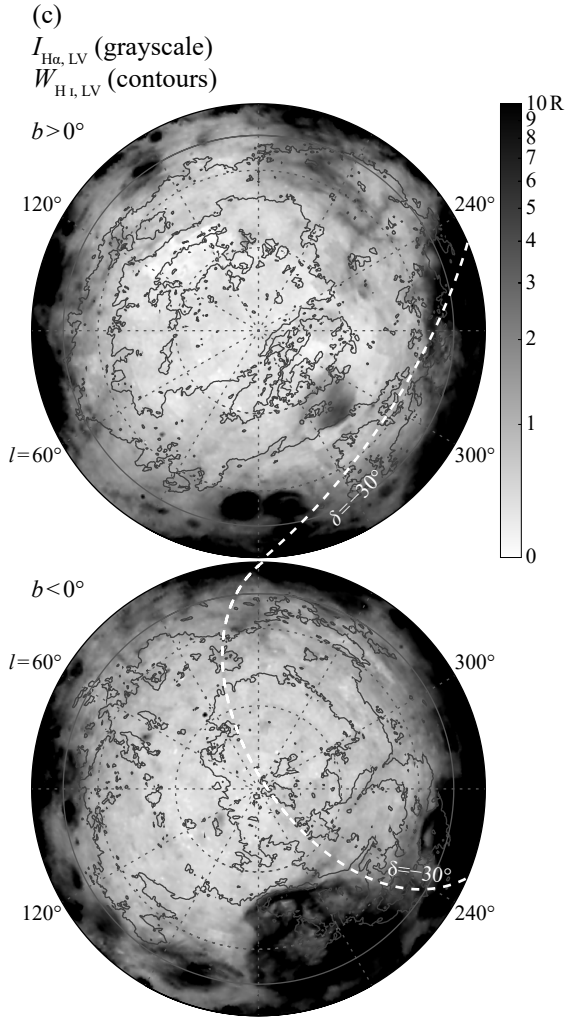


Figure 16 – *continued* (c) Spatial distribution of $I_{\text{H}\alpha}$ in the LV. The contours show $W_{\text{H}\alpha, \text{LV}} = 30, 100, \text{ and } 300 \text{ K km s}^{-1}$.

accretion of the halo gas onto the IVCs. The accretion increases the metallicity and mass of the IVCs and decelerates their infall velocity, as shown by the theoretical work. Therefore, the observed fraction of the low metallicity IVCs gives a secure lower limit for the fraction. By the interaction, the IVC mass will be doubled accompanying a decrease of the infall velocity by a factor of 2 by the momentum conservation as well as the increase of the metallicity. This suggests that the fraction of the observed low metallicity IVCs should be doubled to 40 per cent prior to the onset of the collisional interaction in the halo. Consequently, we suggest an overall picture that both the external infall and the Galactic fountain work to produce the IVCs, where the mass of the IVCs involved is comparable between the two mechanisms.

(iii) To pursue further the implications of the IVCs, we need more systematic studies of the H I gas over the whole sky by focusing on the individual regions and the overall properties of the IVCs and HVCs. The forthcoming new instruments, including SKA and ngVLA, are expected to provide important opportunities in these studies by covering the Local Group galaxies and nearby and more distant galaxies.

ACKNOWLEDGEMENTS

This work was supported by JSPS KAKENHI Grant Numbers JP15H05694 and JP21H00040. This research made use of ds9, a tool for data visualisation supported by the Chandra X-ray Science Center (CXC) and the High Energy Astrophysics Science Archive Center (HEASARC) with support from the JWST Mission office at the Space Telescope Science Institute for 3D visualisation. The valuable comments by Professors T. Onishi, K. Tachihara, A. Mizuno and T. Inoue helped to improve the content and readability of the paper. We also thank the anonymous reviewers for their careful reading of our manuscript and their many valuable comments and suggestions.

DATA AVAILABILITY

The HI4PI data underlying this article are available in VizierR at <http://cdsarc.u-strasbg.fr/viz-bin/qcat?J/A+A/594/A116>. The *Planck* data are in Planck Legacy Archive (PLA) at <https://pla.esac.esa.int/>. The WHAM-SS data are available at <https://www.astro.wisc.edu/research/research-areas/galactic-astronomy/wham/wham-sky-survey/wham-ss-data-release/>. The data products from this study will be shared on reasonable request to the corresponding author.

REFERENCES

- Asplund M., Grevesse N., Sauval A. J., Scott P., 2009, *ARA&A*, **47**, 481
- Barger K. A., Haffner L. M., Wakker B. P., Hill A. S., Madsen G. J., Duncan A. K., 2012, *ApJ*, **761**, 145
- Barger K. A., et al., 2017, *ApJ*, **851**, 110
- Blaauw A., Tolbert C. R., 1966, *Bull. Astron. Inst. Netherlands*, **18**, 405
- Bregman J. N., 1980, *ApJ*, **236**, 577
- Brunsdon C., Fotheringham A. S., Charlton M. E., 1996, *Geographical Analysis*, **28**, 281
- Casandjian J.-M., Ballet J., Grenier I., Remy Q., 2022, *ApJ*, **940**, 116
- Cashman F. H., et al., 2023, *ApJ*, **944**, 65
- Collins J. A., Shull J. M., Giroux M. L., 2003, *ApJ*, **585**, 336
- Collins J. A., Shull J. M., Giroux M. L., 2007, *ApJ*, **657**, 271
- Danly L., Albert C. E., Kuntz K. D., 1993, *ApJ*, **416**, L29
- De Vis P., et al., 2019, *A&A*, **623**, A5
- Dobler G., Draine B., Finkbeiner D. P., 2009, *ApJ*, **699**, 1374
- Finkbeiner D. P., 2003, *ApJS*, **146**, 407
- Fitzpatrick E. L., Spitzer Lyman J., 1997, *ApJ*, **475**, 623
- Fotheringham A. S., Brunsdon C., Charlton M., 2002, *Geographically Weighted Regression: the analysis of spatially varying relationships*. Wiley
- Fox A. J., Wakker B. P., Smoker J. V., Richter P., Savage B. D., Sembach K. R., 2010, *ApJ*, **718**, 1046
- Fox A. J., Richter P., Wakker B. P., Lehner N., Howk J. C., Ben Bekhti N., Bland-Hawthorn J., Lucas S., 2013, *ApJ*, **772**, 110
- Fox A. J., et al., 2016, *ApJ*, **816**, L11
- Fox A. J., Cashman F. H., Kriss G. A., de Rosa G., Plesha R., Homayouni Y., Richter P., 2023, *ApJ*, **946**, L48
- French D. M., et al., 2021, *ApJ*, **923**, 50
- Fukui Y., et al., 2014, *ApJ*, **796**, 59
- Fukui Y., Torii K., Onishi T., Yamamoto H., Okamoto R., Hayakawa T., Tachihara K., Sano H., 2015, *ApJ*, **798**, 6
- Fukui Y., Tsuge K., Sano H., Bekki K., Yozin C., Tachihara K., Inoue T., 2017, *PASJ*, **69**, L5
- Fukui Y., et al., 2021, *PASJ*, **73**, S117
- Gibson B. K., Giroux M. L., Penton S. V., Putman M. E., Stocke J. T., Shull J. M., 2000, *AJ*, **120**, 1830

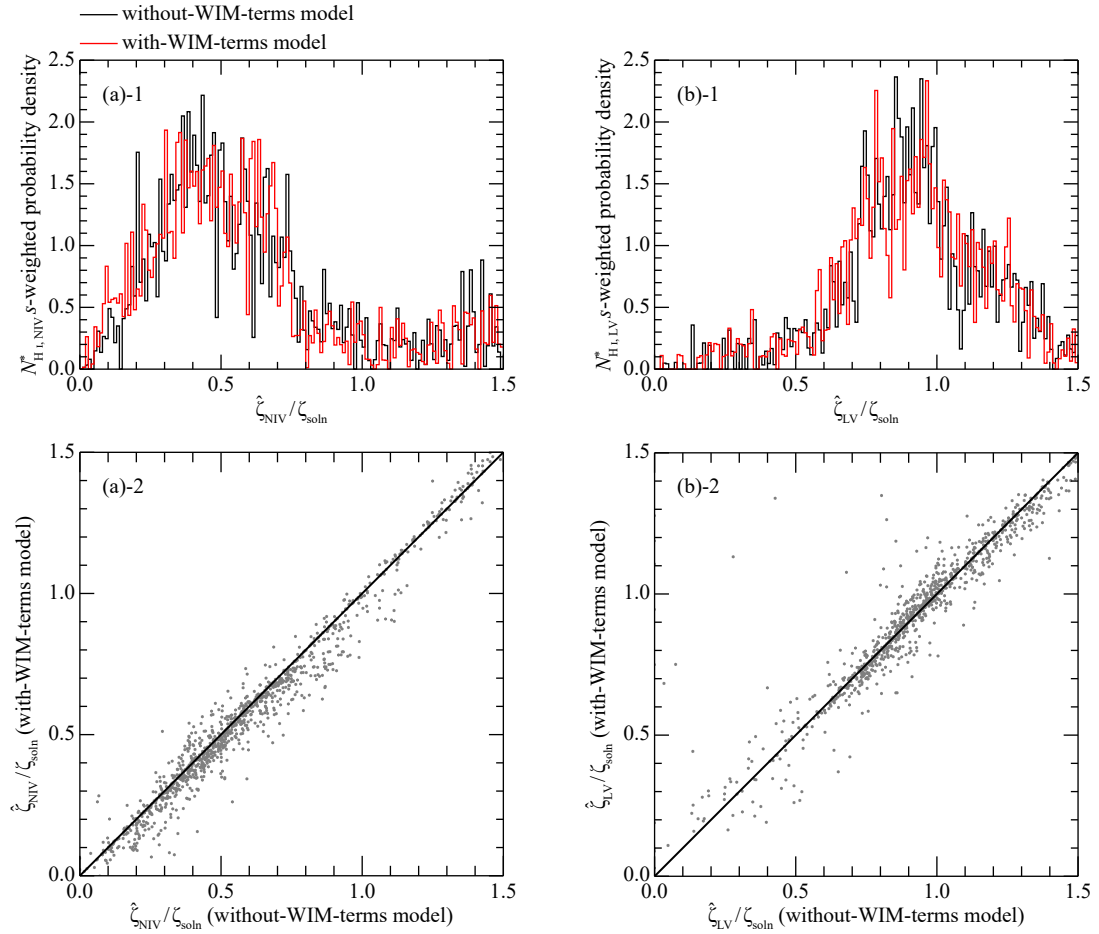


Figure 17. (a)-1 The black and red lines show the $N_{\text{H I, NIV}}^*$ -weighted probability density with respect to $\hat{\zeta}_{\text{NIV}}/\zeta_{\text{soln}}$ obtained using the “without-WIM-terms” and “with-WIM-terms” models, respectively (see Section 5.2). (a)-2 Scatter plot showing a correlation between $\hat{\zeta}_{\text{NIV}}/\zeta_{\text{soln}}$ (without-WIM-terms model) and $\hat{\zeta}_{\text{NIV}}/\zeta_{\text{soln}}$ (with-WIM-terms model). The solid line shows the line where both have the same value. (b) Same as (a) but for $\hat{\zeta}_{\text{LV}}/\zeta_{\text{soln}}$.

Górski K. M., Hivon E., Banday A. J., Wandelt B. D., Hansen F. K., Reinecke M., Bartelmann M., 2005, *ApJ*, **622**, 759
 Gritton J. A., Shelton R. L., Galyardt J. E., 2017, *ApJ*, **842**, 102
 HI4PI Collaboration 2016, *A&A*, **594**, A116
 Haffner L. M., Reynolds R. J., Tuftte S. L., 2001, *ApJ*, **556**, L33
 Haffner L. M., Reynolds R. J., Tuftte S. L., Madsen G. J., Jaehnig K. P., Percival J. W., 2003, *ApJS*, **149**, 405
 Haffner L. M., et al., 2010, in Kothes R., Landecker T. L., Willis A. G., eds, *Astronomical Society of the Pacific Conference Series Vol. 438, The Dynamic Interstellar Medium: A Celebration of the Canadian Galactic Plane Survey*. p. 388 ([arXiv:1008.0612](https://arxiv.org/abs/1008.0612))
 Hayashi K., Okamoto R., Yamamoto H., Hayakawa T., Tachihara K., Fukui Y., 2019a, *ApJ*, **878**, 131
 Hayashi K., et al., 2019b, *ApJ*, **884**, 130
 Henley D. B., Gritton J. A., Shelton R. L., 2017, *ApJ*, **837**, 82
 Howk J. C., Savage B. D., 1999, *ApJ*, **517**, 746
 Isobe T., Feigelson E. D., Akritas M. G., Babu G. J., 1990, *ApJ*, **364**, 104
 Kalberla P. M. W., Haud U., 2015, *A&A*, **578**, A78
 Kalberla P. M. W., Burton W. B., Hartmann D., Arnal E. M., Bajaja E., Morras R., Pöppel W. G. L., 2005, *A&A*, **440**, 775
 Karachentsev I. D., Makarov D. I., Kaisina E. I., 2013, *AJ*, **145**, 101
 Kunth D., Lequeux J., Sargent W. L. W., Viallefond F., 1994, *A&A*, **282**, 709
 Lagache G., Abergel A., Boulanger F., Désert F. X., Puget J. L., 1999, *A&A*, **344**, 322
 Lagache G., Haffner L. M., Reynolds R. J., Tuftte S. L., 2000, *A&A*, **354**, 247
 Lawson C. L., Hanson R. J., 1995, *Solving least squares problems*. SIAM,

Philadelphia, PA, doi:<https://doi.org/10.1137/1.9781611971217>
 Lehner N., Howk J. C., 2011, *Science*, **334**, 955
 Lehner N., Howk J. C., Marasco A., Fraternali F., 2022, *MNRAS*, **513**, 3228
 Lenz D., Flöer L., Kerp J., 2016, *A&A*, **586**, A121
 Miville-Deschênes M. A., Boulanger F., Reach W. T., Noriega-Crespo A., 2005, *ApJ*, **631**, L57
 Muller C. A., Oort J. H., Raimond E., 1963, *Academie des Sciences Paris Comptes Rendus*, **257**, 1661
 Munch G., 1952, *PASP*, **64**, 312
 Münch G., Zirin H., 1961, *ApJ*, **133**, 11
 Odegard N., Arendt R. G., Dwek E., Haffner L. M., Hauser M. G., Reynolds R. J., 2007, *ApJ*, **667**, 11
 Okamoto R., Yamamoto H., Tachihara K., Hayakawa T., Hayashi K., Fukui Y., 2017, *ApJ*, **838**, 132
 Peek J. E. G., Heiles C., Putman M. E., Douglas K., 2009, *ApJ*, **692**, 827
 Planck Collaboration XI 2014, *A&A*, **571**, A11
 Planck Collaboration X 2016, *A&A*, **594**, A10
 Planck Collaboration Int. XLVIII 2016, *A&A*, **596**, A109
 Richter P., Savage B. D., Wakker B. P., Sembach K. R., Kalberla P. M. W., 2001a, *ApJ*, **549**, 281
 Richter P., Sembach K. R., Wakker B. P., Savage B. D., Tripp T. M., Murphy E. M., Kalberla P. M. W., Jenkins E. B., 2001b, *ApJ*, **559**, 318
 Richter P., Fox A. J., Wakker B. P., Lehner N., Howk J. C., Bland-Hawthorn J., Ben Bekhti N., Fechner C., 2013, *ApJ*, **772**, 111
 Richter P., de Boer K. S., Werner K., Rauch T., 2015, *A&A*, **584**, L6
 Rocha-Pinto H. J., Maciel W. J., 1996, *MNRAS*, **279**, 447

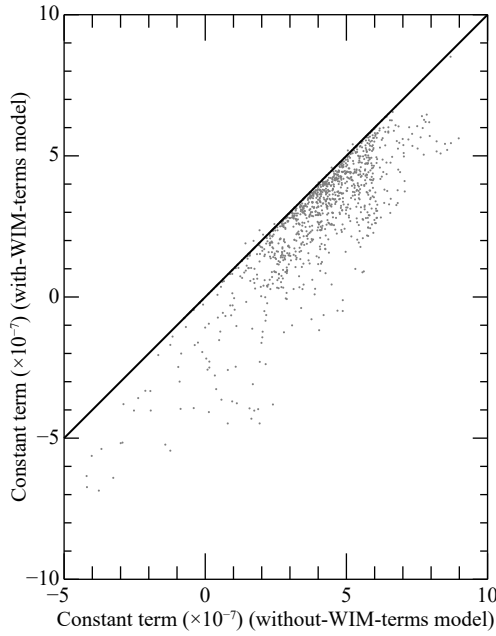


Figure 18. Scatter plot showing a correlation between constant term values of the “without-WIM-terms model” and those of the “with-WIM-terms model”. The solid line shows the line where both have the same value.

- Röhser T., Kerp J., Lenz D., Winkel B., 2016, *A&A*, 596, A94
 Roy A., et al., 2013, *ApJ*, 763, 55
 Saul D. R., Peek J. E. G., Putman M. E., 2014, *MNRAS*, 441, 2266
 Sembach K. R., et al., 2003, *ApJS*, 146, 165
 Sembach K. R., et al., 2004, *ApJS*, 150, 387
 Shapiro P. R., Field G. B., 1976, *ApJ*, 205, 762
 Shull J. M., Jones J. R., Danforth C. W., Collins J. A., 2009, *ApJ*, 699, 754
 Smith G. P., 1963, *Bull. Astron. Inst. Netherlands*, 17, 203
 Smoker J. V., Fox A. J., Keenan F. P., 2011, *MNRAS*, 415, 1105
 Spitzer Lyman J., Fitzpatrick E. L., 1993, *ApJ*, 409, 299
 Thom C., Putman M. E., Gibson B. K., Christlieb N., Flynn C., Beers T. C., Wilhelm R., Lee Y. S., 2006, *ApJ*, 638, L97
 Thom C., Peek J. E. G., Putman M. E., Heiles C., Peek K. M. G., Wilhelm R., 2008, *ApJ*, 684, 364
 Tripp T. M., et al., 2003, *AJ*, 125, 3122
 Tsuge K., et al., 2019, *ApJ*, 871, 44
 Tuftle S. L., Reynolds R. J., Haffner L. M., 1998, *ApJ*, 504, 773
 Wakker B. P., 1991, *A&A*, 250, 499
 Wakker B. P., 2001, *ApJS*, 136, 463
 Wakker B. P., Boulanger F., 1986, *A&A*, 170, 84
 Wakker B. P., de Boer K. S., van Woerden H., 2004, in van Woerden H., Wakker B. P., Schwarz U. J., de Boer K. S., eds, *Astrophysics and Space Science Library* Vol. 312, High Velocity Clouds. p. 1, doi:10.1007/1-4020-2579-3_1
 Wakker B. P., et al., 2007, *ApJ*, 670, L113
 Wakker B. P., York D. G., Wilhelm R., Barentine J. C., Richter P., Beers T. C., Ivezić Ž., Howk J. C., 2008, *ApJ*, 672, 298
 Wang J., Koribalski B. S., Serra P., van der Hulst T., Roychowdhury S., Kamphuis P., Chengalur J. N., 2016, *MNRAS*, 460, 2143
 Werk J. K., et al., 2019, *ApJ*, 887, 89
 Winkel B., Kerp J., Flöer L., Kalberla P. M. W., Ben Bekhti N., Keller R., Lenz D., 2016, *A&A*, 585, A41
 van Woerden H., Wakker B. P., 2004, *Distances and Metallicities of HVCS*. p. 195, doi:10.1007/1-4020-2579-3_10
 van Woerden H., Schwarz U. J., Peletier R. F., Wakker B. P., Kalberla P. M. W., 1999, *Nature*, 400, 138

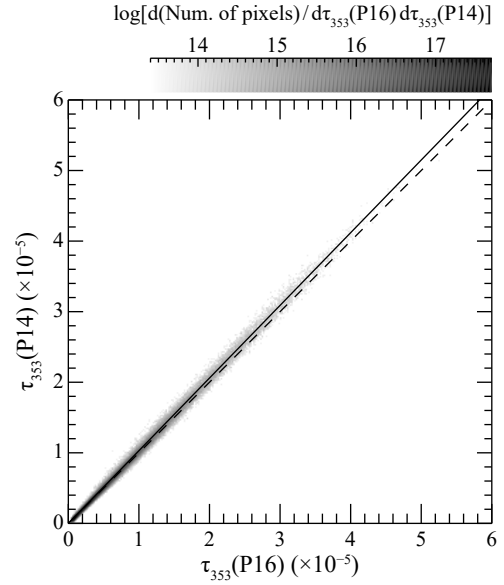


Figure A1. Density plot showing a correlation between $\tau_{353}(\text{P16})$ and $\tau_{353}(\text{P14})$. The solid line shows the linear regression line (equation (A1)) and the dashed line shows $\tau_{353}(\text{P14}) = \tau_{353}(\text{P16})$.

APPENDIX A: CONSISTENCY OF THE PR2 DUST DATA WITH THE PR1 DATA

We checked the consistency between *Planck* PR2 GNILC dust data (released version R2.01, *Planck Collaboration Int. XLVIII 2016*, refer to it as the P16 data in this section) and PR1 data (R1.20, *Planck Collaboration XI 2014*, the P14 data). Here, we did not smooth the P16 data but smoothed the P14 data to have the same effective beam size as the original P16 data. Then both were degraded to $N_{\text{side}} = 256$. Here, we applied the masking criteria (a)–(c) in Section 4.1.

Fig. A1 shows the $\tau_{353}(\text{P16})$ – $\tau_{353}(\text{P14})$ correlation. The two datasets are highly correlated with a correlation coefficient of 0.999 and a linear regression by an OLS-bisector method (*Isobe et al. 1990*) is

$$\tau_{353}(\text{P14}) = (1.0297 \pm 0.0002) \times \tau_{353}(\text{P16}) - (8.74 \pm 0.07) \times 10^{-8}. \quad (\text{A1})$$

We found a good consistency between $\tau_{353}(\text{P16})$ and $\tau_{353}(\text{P14})$.

APPENDIX B: GEOGRAPHICALLY WEIGHTED REGRESSION ANALYSIS

B1 Estimating the local coefficients

Prior to the analysis, we performed a linearizing transformation on $W_{\text{HI},k}$ ($k = 1, \dots, m$; $m = 5$ in the present study and corresponding to the five velocity ranges in Table 1)

$$x_k(l_i, b_i) = \begin{cases} [W_{\text{HI},k}(l_i, b_i)]^\alpha & \text{if } W_{\text{HI},k}(l_i, b_i) > 5.5 \text{ K km s}^{-1} \\ 0 & \text{otherwise} \end{cases} \quad (\text{B1})$$

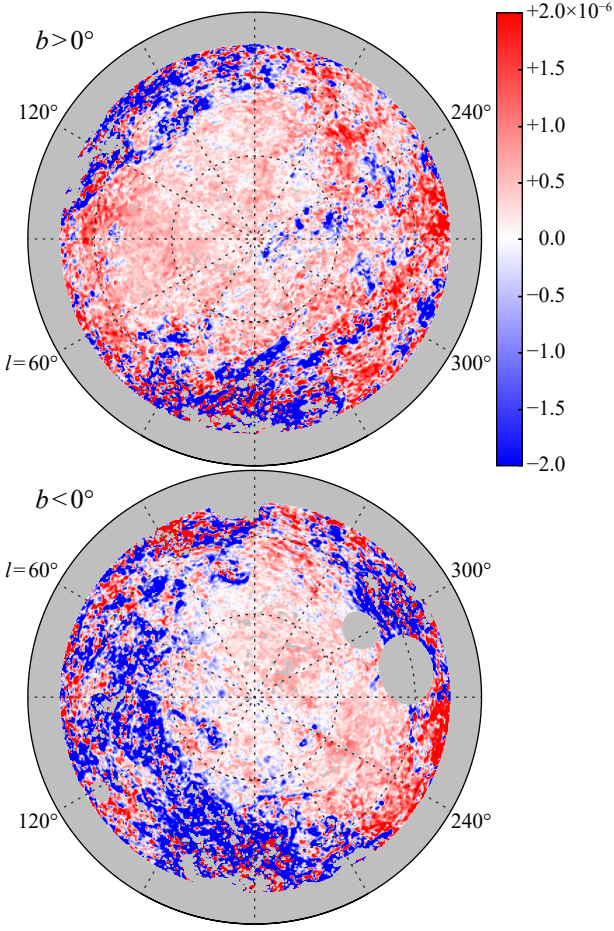


Figure B1. Spatial distribution of $\widehat{\tau}_{353,0}$ shown in the same projection as Fig. 2.

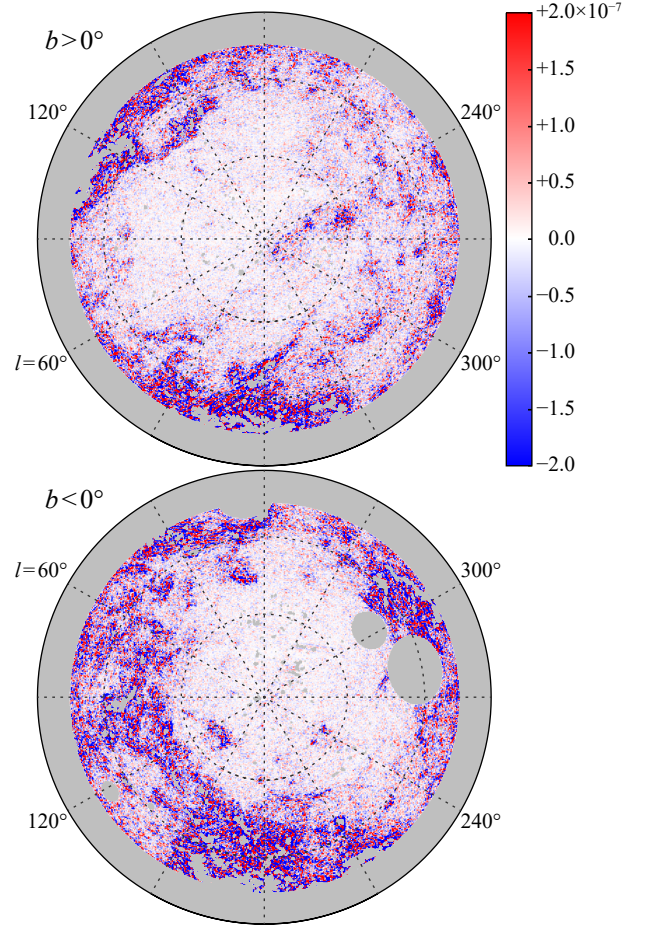


Figure B2. Spatial distribution of the residual from the regression shown in the same projection as Fig. 2.

and replaced other variables,

$$y(l_i, b_i) = C_0^{-\alpha} \tau_{353}(l_i, b_i) \quad (\text{B2})$$

$$a(l_i, b_i) = C_0^{-\alpha} \tau_{353,0}(l_i, b_i) \quad (\text{B3})$$

$$\beta_k(l_i, b_i) = [\zeta_k(l_i, b_i)]^\alpha. \quad (\text{B4})$$

Equation (8) was rewritten as

$$y(l_i, b_i) = a(l_i, b_i) + \sum_{k=1}^m [\beta_k(l_i, b_i) x_k(l_i, b_i)] + \varepsilon(l_i, b_i), \quad (\text{B5})$$

where $\varepsilon(l_i, b_i)$ is the error term. Equation (B5) can be rewritten in a matrix form

$$\mathbf{y} = \mathbf{a} + (\mathbf{B} \circ \mathbf{X}) \mathbf{1}_{m \times n} + \boldsymbol{\varepsilon}, \quad (\text{B6})$$

where \circ denotes the Hadamard product (also known as element-wise product) of the matrices,

$$\mathbf{X} = \begin{bmatrix} x_1(l_1, b_1) & \cdots & x_m(l_1, b_1) \\ \vdots & \ddots & \vdots \\ x_1(l_n, b_n) & \cdots & x_m(l_n, b_n) \end{bmatrix}, \quad (\text{B7})$$

is the matrix of the n observations of m independent variables,

$$\mathbf{B} = \begin{bmatrix} \beta_1(l_1, b_1) & \cdots & \beta_m(l_1, b_1) \\ \vdots & \ddots & \vdots \\ \beta_1(l_n, b_n) & \cdots & \beta_m(l_n, b_n) \end{bmatrix} = \begin{bmatrix} \boldsymbol{\beta}(l_1, b_1)^T \\ \vdots \\ \boldsymbol{\beta}(l_n, b_n)^T \end{bmatrix} \quad (\text{B8})$$

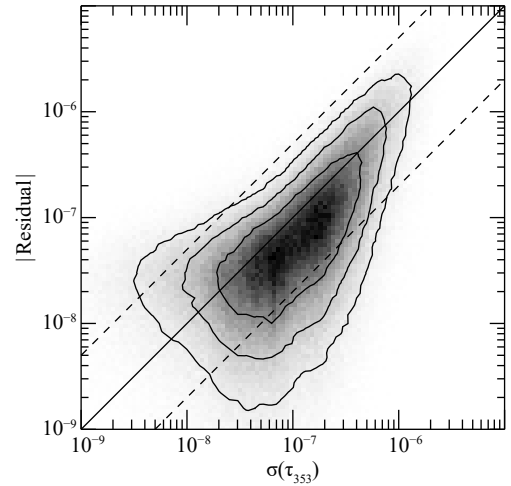


Figure B3. Density plot showing the correlation between $\sigma(\tau_{353})$ (Planck Collaboration Int. XLVIII 2016) and absolute values of the residuals from the regression. The solid line shows the line where both have the same value, and the dashed lines show $|\text{Residual}| = 0.5 \sigma \tau_{353}$ and $2 \sigma \tau_{353}$. The contours contain 50, 75 and 90 per cent of data points.

is n set of local coefficients, and $\mathbf{1}_{m \times n}$ is an $m \times n$ all-ones matrix. The n -element vectors \mathbf{y} , \mathbf{a} , and $\boldsymbol{\varepsilon}$ are dependent variables, local constant terms, and error terms.

The local regression coefficients at the i -th regression point are given by solving

$$\widehat{\boldsymbol{\beta}}_i = (\mathbf{X}_i^T \mathbf{W}_i \mathbf{X}_i)^{-1} \mathbf{X}_i^T \mathbf{W}_i \mathbf{y}_i, \quad (\text{B9})$$

where

$$\mathbf{X}_i = (\mathbf{I}_n - \mathbf{W}_i \mathbf{1}_{n \times n}) \mathbf{X} \quad (\text{B10})$$

is the matrix of the local-centred independent variables,

$$\mathbf{y}_i = (\mathbf{I}_n - \mathbf{W}_i \mathbf{1}_{n \times n}) \mathbf{y}, \quad (\text{B11})$$

is the local-centred dependent variable, \mathbf{I}_n is the identity matrix of size n , $\mathbf{1}_{n \times n}$ is an $n \times n$ all-ones matrix, $\boldsymbol{\beta}_i$ is a short-hand notation for $\boldsymbol{\beta}(l_i, b_i)$, the superscript T indicates the matrix transpose, \mathbf{W}_i is a weighting matrix

$$\mathbf{W}_i = \frac{1}{\sum_{j=1}^n w_i(l_j, b_j)} \begin{bmatrix} w_i(l_1, b_1) & & \\ & \ddots & \\ & & w_i(l_n, b_n) \end{bmatrix}, \quad (\text{B12})$$

and $w_i(l_j, b_j)$ is given by equation (9). As each component of $\boldsymbol{\beta}_i$ should be non-negative ($\boldsymbol{\beta}_i \geq 0$), equation (B9), therefore, must be reformulated by a NNLS problem

$$\text{Minimize } \|\mathbf{W}_i (\mathbf{X}_i \boldsymbol{\beta}_i - \mathbf{y}_i)\| \text{ subject to } \boldsymbol{\beta}_i \geq 0, \quad (\text{B13})$$

where $\|\cdot\|$ denotes Euclidean norm (or also called L^2 norm). A widely used algorithm for solving NNLS problems is the one by [Lawson & Hanson \(1995\)](#) briefly summarized as follows.

1. Initialize set $P = \emptyset$ and $Q = \{1, \dots, m\}$.
2. Let $\mathbf{u} = (u_1 \ \dots \ u_m) = \mathbf{X}_i^T (\mathbf{y}_i - \mathbf{X}_i \boldsymbol{\beta}_i)$.
3. If $Q = \emptyset$ or $\max\{u_q : q \in Q\} \leq 0$, the calculation is completed.
4. Find an index $k \in Q$ such that $u_k = \max\{u_q : q \in Q\}$, and then move the index k from Q to P .
5. Let \mathbf{P}_i denote the $n \times m$ matrix defined by

$$\text{column } k \text{ of } \mathbf{P}_i = \begin{cases} \text{column } k \text{ of } \mathbf{X}_i & \text{if } k \in P \\ 0 & \text{if } k \in Q. \end{cases} \quad (\text{B14})$$

6. Let \mathbf{z} be vector of same length as $\boldsymbol{\beta}_i$, and set

$$\mathbf{z} = (z_1 \ \dots \ z_m) = (\mathbf{P}_i^T \mathbf{P}_i)^{-1} \mathbf{P}_i^T \mathbf{y}. \quad (\text{B15})$$

7. Set $z_q = 0$ for $q \in Q$.
8. If $\min\{z_p : p \in P\} > 0$, set $\boldsymbol{\beta}_i = \mathbf{z}$ and go to Step 2.
9. Let

$$\gamma = \min \left\{ \frac{\beta_p}{\beta_p - z_p} : z_p \leq 0, p \in P \right\}, \quad (\text{B16})$$

where β_p means the p -th element of $\boldsymbol{\beta}_i$.

10. Set $\boldsymbol{\beta}_i$ to $\boldsymbol{\beta}_i + \gamma(\mathbf{z} - \boldsymbol{\beta}_i)$.
11. Move from P to Q all indices $p \in P$ such that $\beta_p \leq 0$. Then go to Step 5.

The obtained $\boldsymbol{\beta}_i$ satisfies $\beta_p > 0$ for $p \in P$, $\beta_q = 0$ for $q \in Q$, and is an estimator $\widehat{\boldsymbol{\beta}}_i$ for the least squares problem

$$\mathbf{P}_i \boldsymbol{\beta}_i = \mathbf{y}_i. \quad (\text{B17})$$

The estimator of the constant term is given by

$$\widehat{a}(l_i, b_i) = \mathbf{1}_{1 \times n} \mathbf{W}_i \left[\mathbf{y} - \mathbf{X} \widehat{\boldsymbol{\beta}}_i \right], \quad (\text{B18})$$

where $\mathbf{1}_{1 \times n}$ is an n -element all-ones row vector.

The estimated regression coefficients are transformed as following

$$\widehat{\zeta}_k(l_i, b_i) = \left[\widehat{\beta}_k(l_i, b_i) \right]^{1/\alpha} \quad (\text{B19})$$

$$\widehat{\tau}_{353,0}(l_i, b_i) = C_0^\alpha \widehat{a}(l_i, b_i). \quad (\text{B20})$$

Figs. B1 and Fig. B2 shows the constant term $\widehat{\tau}_{353,0}$ and the residual from the regression given by $\tau_{353}(l_i, b_i) - \widehat{\tau}_{353}(l_i, b_i)$, respectively. Fig. B3 shows that the residuals are comparable to $\sigma(\tau_{353})$, indicating the goodness-of-fit. The residuals tend to be somewhat smaller, probably due to the smoothing applied to the H I data (see Section 2.3).

B2 The standard error of the estimated local coefficients

Let

$$\mathbf{C}_i = (\mathbf{P}_i^T \mathbf{W}_i \mathbf{P}_i)^{-1} \mathbf{P}_i^T \mathbf{W}_i, \quad (\text{B21})$$

where \mathbf{P}_i satisfies

$$\text{column } k \text{ of } \mathbf{P}_i = \begin{cases} \text{column } k \text{ of } \mathbf{X}_i & \text{if the } k\text{-th element of } \widehat{\boldsymbol{\beta}}_i > 0 \\ 0 & \text{if the } k\text{-th element of } \widehat{\boldsymbol{\beta}}_i = 0 \end{cases} \quad (\text{B22})$$

Then the estimated variance-covariance matrix of $\widehat{\boldsymbol{\beta}}(l_i, b_i)$ is denoted by

$$\mathbf{V}_i = \sigma^2 \mathbf{C}_i \mathbf{C}_i^T, \quad (\text{B23})$$

where σ^2 is the normalized residual sum of squares (RSS) from the local regression

$$\sigma^2 = \frac{(\mathbf{y}_i - \widehat{\mathbf{y}}_i)^T \mathbf{W}_i (\mathbf{y}_i - \widehat{\mathbf{y}}_i)}{n - 2\text{tr}\mathbf{S} + \text{tr}(\mathbf{S}^T \mathbf{S})} \sim \frac{(\mathbf{y}_i - \widehat{\mathbf{y}}_i)^T \mathbf{W}_i (\mathbf{y}_i - \widehat{\mathbf{y}}_i)}{n - \text{tr}\mathbf{S}}, \quad (\text{B24})$$

where $\widehat{\mathbf{y}}_i = \mathbf{P}_i \widehat{\boldsymbol{\beta}}_i$. The matrix \mathbf{S} is the hat matrix which maps $\widehat{\mathbf{y}}_i$ on to \mathbf{y}_i

$$\widehat{\mathbf{y}}_i = \mathbf{S} \mathbf{y}_i, \quad (\text{B25})$$

and the i -th row of \mathbf{S} is given by

$$s_i = (\text{row } i \text{ of } \mathbf{P}_i) \mathbf{C}_i. \quad (\text{B26})$$

The standard errors of the components of $\widehat{\boldsymbol{\beta}}(l_i, b_i)$, $\sigma \left[\widehat{\beta}_k(l_i, b_i) \right]$ are obtained from square roots of diagonal elements of \mathbf{V}_i . The estimated standard errors are transformed as

$$\sigma(\widehat{\zeta}_k)(l_i, b_i) = \frac{1}{\alpha} \widehat{\beta}_k \left[\widehat{\beta}_k(l_i, b_i) \right]^{1/\alpha - 1} \sigma \left[\widehat{\beta}_k(l_i, b_i) \right]. \quad (\text{B27})$$

Fig. B4 shows that $\sigma(\widehat{\zeta}_X)$ is inversely proportional to $W_{\text{H I}, X}$, this is because ζ_X are the gradient of the plane in the τ_{353} - $W_{\text{H I}, X}$ space. The closer to the origin, the higher- ζ_X - and lower- ζ_X planes become close.

This paper has been typeset from a $\text{\TeX}/\text{\LaTeX}$ file prepared by the author.

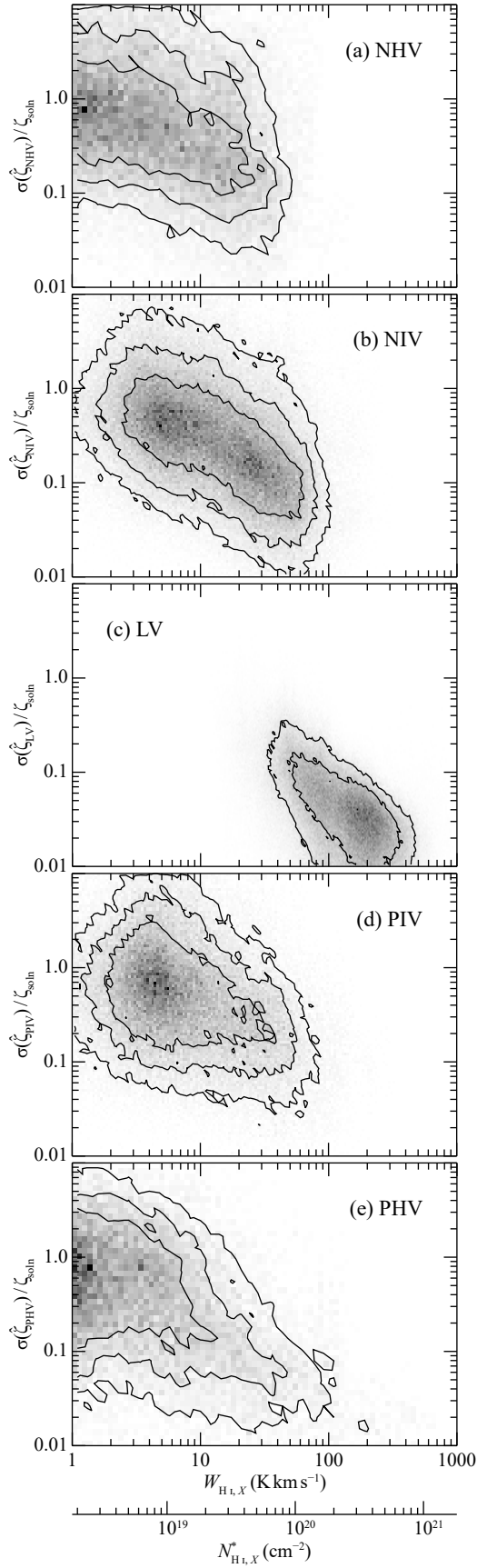


Figure B4. Density plot showing the correlation between $\sigma(\widehat{\zeta}_X)/\zeta_{\text{soln}}$ and $W_{\text{H I},X}$ in (a) NHV, (b) NIV, (c) LV, (d) PIV, and (e) PHV. The contours contain 50, 75, and 90 per cent of data points.